

The Pennsylvania State University  
The Graduate School  
College of Engineering

NONDESTRUCTIVE FORENSIC PATHOLOGY OF LEAD-ACID BATTERIES

A Thesis in  
Mechanical Engineering  
by  
Christopher A. Ferone

© 2012 Christopher A. Ferone

Submitted in Partial Fulfillment  
of the Requirements  
for the Degree of

Master of Science

May 2012

The thesis of Christopher A. Ferone was reviewed and approved\* by the following:

Christopher D. Rahn  
Professor of Mechanical Engineering  
Thesis Advisor

Hosam Fathy  
Professor of Mechanical Engineering

Karen A. Thole  
Professor of Mechanical Engineering  
Head of the Department of Mechanical Engineering and Nuclear Engineering

\*Signatures are on file in the Graduate School.

# Abstract

Valve Regulated Lead-Acid (VRLA) batteries can degrade due to a variety of mechanisms, including corrosion, hard sulfation, water loss, shedding, and active mass degradation. VRLA batteries are designed to minimize these effects as much as possible but the operating environment, cell-to-cell and battery-to-battery manufacturing variations, and use can cause different degradation mechanisms to dominate capacity loss and/or impedance rise. With accurate State of Health monitoring, cell usage can be adjusted by the battery management system (BMS) to optimize the performance and life of the energy storage system. The BMS must be able to determine in real-time the predominant degradation mechanism for each cell and adjust use accordingly. In this paper, new and dead VRLA batteries are tested with constant, sinusoidal, and pulse charge/discharge current inputs while measuring the cell voltage and pressure to determine the cause of death of the cells. As expected, the new cells have fairly uniform performance with limited signs of degradation. The cells in the dead battery, however, have widely ranging performance, especially at the end of discharge and charge. Analysis of the charge/discharge data indicate that two cells died of water loss and a third cell died of sulfation. The remaining three cells were fairly healthy but will accompany their dead companions to the recycling center nonetheless. While the full charge/discharge data provided useful forensic pathology data, EIS

and pulse charge/discharge data varied with aging mechanism but the correlation was unclear.

# Table of Contents

<b>List of Figures</b>	<b>vii</b>
<b>List of Tables</b>	<b>ix</b>
<b>Acknowledgments</b>	<b>x</b>
<b>Chapter 1</b>	
<b>Nondestructive Forensic Pathology of Lead-Acid Batteries</b>	<b>1</b>
1.1 Introduction . . . . .	1
1.2 Experimental Procedure . . . . .	4
1.2.1 Battery Cycling . . . . .	4
1.2.2 Full Charge/Discharge and Pulse Train Testing . . . . .	4
1.2.3 Impedance Testing . . . . .	5
1.3 Results and Discussion . . . . .	7
1.3.1 Full Charge/Discharge Testing . . . . .	7
1.3.2 Pulse Train Testing . . . . .	9
1.3.3 Impedance Testing . . . . .	11
1.4 Conclusions . . . . .	11
<b>Appendix A</b>	
<b>Battery Testing Hardware</b>	<b>14</b>
A.1 Power Supplies and Grounding . . . . .	15
A.1.1 Power Supplies . . . . .	15
A.1.2 Grounding . . . . .	16
A.2 Voltage Measurement . . . . .	19
A.2.1 Amplifier Voltage Measurement . . . . .	19
A.2.2 Battery and Cell Voltage Measurement . . . . .	20
A.3 Sensors . . . . .	23
A.3.1 Current Sensor . . . . .	23
A.3.2 Pressure and Temperature Sensors . . . . .	26
A.4 Relays . . . . .	26
A.4.1 Battery-Amplifier “Handshake” . . . . .	27
A.5 Battery Charging and Discharging . . . . .	27

A.5.1	Discharging . . . . .	28
A.5.2	Charging . . . . .	31
A.5.3	Amplifier Configuration and Settings . . . . .	32
A.6	Voltage, Current, and Pressure Control . . . . .	33
A.7	Impedance Measurement . . . . .	36
A.7.1	First Generation EIS Circuit . . . . .	38
A.7.2	Second Generation EIS Circuit . . . . .	39
A.7.3	Third Generation EIS Circuit . . . . .	41
A.8	Safety Features . . . . .	43
<b>Appendix B</b>		
<b>Circuit Diagrams</b>		<b>44</b>
<b>Bibliography</b>		<b>48</b>

# List of Figures

1.1	VRLA Battery Configuration: Six cells in chambers 1 - 6 are individually sealed and connected in series through current collectors. . . . .	3
1.2	Photograph of the experimental setup. . . . .	5
1.3	Charge/discharge of the new battery: (a) Cell pressure during charge; (b) Cell pressure during discharge; (c) Cell voltage during charge with inset showing initial distribution; and (d) Cell voltage during discharge with inset showing initial distribution. . . . .	6
1.4	Charge/discharge of the dead battery: (a) Cell pressure during charge with inset showing pressure build-up; (b) Cell pressure during discharge; (c) Cell voltage during charge with inset showing initial distribution with inset (i) showing the initial distribution and (ii) showing voltage change at the end of charge; and (d) Cell voltage during discharge with inset showing initial distribution. . . . .	7
1.5	Pulse train voltage response of the new (a) and aged (b) batteries. The OCV of each cell was subtracted from each curve to facilitate comparisons between cells. . . . .	10
1.6	EIS plots of the new (a) and aged (b) batteries from 0.01Hz to 100Hz. . . . .	13
A.1	The PBTM is shown below the amplifier and above the DAQ system. . . . .	15
A.2	PCB Power supply . . . . .	17
A.3	SL Power GECA20-12G 12V Power supply . . . . .	17
A.4	The DAQ ground lead (blue wire) is not connected to the amplifier output signal ground (green wire) to avoid hum and noise problems. Ground isolation also ensures that the current flowing into the low side of the ADC input channel is equal to the current flowing out of the high side, i.e. $i_L = i_H$ . . . . .	18
A.5	Amplifier voltage is measured by taking the difference between $V_{amp(+)/DAQ}$ and $V_{amp(-)/DAQ}$ . . . . .	19
A.6	Op-amp with adjustable gain used to measure amplifier voltage. . . . .	20
A.7	Circuit used to measure cell voltage. . . . .	22
A.8	The maximum voltage of each electrode relative to the negative battery terminal. . . . .	22
A.9	Current sensor voltage output vs sensed current . . . . .	24
A.10	A CASR 6-NP current sensor. . . . .	25
A.11	A Potter & Brumfield JWD-172-161 DPST reed relay. . . . .	26
A.12	A Panasonic HG2-DC12V-F DPDT 20A power relay. . . . .	26
A.13	Resistors are connected in series and in parallel with the amplifier. Battery current, $i_b$ , is positive when the battery is being charged and negative when the battery is being discharged. Amplifier current, $i_a$ , is positive when the amplifier is sourcing current and negative when the amplifier is sinking current. . . . .	28

A.14	Amplifier current, $i_a$ , as a function of battery current, $i_b$ , for different values of parallel resistance, $R_p$ . The red curve represents $i_a(i_b)$ if no parallel resistor is included in the circuit (i.e. infinite parallel resistance). As $R_p$ decreases and the the y-intercept of the curve $i_a(i_b) = i_b + \frac{V_b}{R_p}$ increases from zero, the maximum amount of current that the amplifier must sink or source decreases until reaching a minimum and then begins to increase. The orange curve, $i_a(i_b) = i_b + 10$ , represents the case where the maximum amount of current that the amplifier must sink or source (i.e. $ i_a $ ) is minimized. . . . .	29
A.15	Ideally amplifier current and voltage should intersect their respective x axes at the same battery current. In other words, amplifier voltage should be zero at the same point that amplifier current is zero. . . . .	30
A.16	A total of $2\Omega$ is connected in series with battery. A $1\Omega$ resistor is connected in parallel as well. . . . .	31
A.17	A total of $1\Omega$ is connected in series with battery. . . . .	32
A.18	The gassing pressure controller consists of two separate control loops. The first controller tracks a pressure derivate set point by varying the current set point. The second tracks the current set point. . . . .	35
A.19	Inverting op-amp with reference signal at non-inverting input . . . . .	38
A.20	Battery Voltage Measurement. . . . .	40
A.21	Battery Voltage Amplitude and Raw Signal Amplitudes. . . . .	42
B.1	Picture of PCB . . . . .	44
B.2	PCB . . . . .	45
B.3	Diagram of Circuits on PCB . . . . .	46
B.4	High level view of PBTM. . . . .	47

# List of Tables

1.1	The radius of curvature of each cell within the aged battery. . . . .	11
-----	---	----

# Acknowledgments

First and foremost, I would like to thank my advisor, Dr. Chris Rahn. More than anything, I am grateful for his patience and understanding during the many months that I struggled to make all of the hardware work. I am so grateful that he gave me the opportunity to work on this project. Despite the setbacks and frustration, I learned so much and had so much fun building hardware from scratch.

I would have never completed this project without the help of the Ying Shi. Many times when I was trying to solve a problem and found myself at a dead end, and was tempted to bang my head against a wall, Ying would work through a problem with me until she was sure that I could move forward. Outside of our discussions relating to work, I enjoyed learning about Chinese culture, tradition, and politics. More than anything, I am grateful to have had the opportunity to work with such a kind and thoughtful person on a daily basis.

I cannot forget to thank all of my graduate school professors who have inspired me and helped me discover what specific areas within the discipline of Mechanical Engineering I truly love. I am grateful to Dr. Sean Brennan for introducing me to mechatronics, to Dr. Hosam Fathy and Dr. Jack Langelaan for teaching me all that I know about feedback control, and to Dr. Karl Reichard for highlighting the importance of understanding Digital Signal Processing.

My interest in studying engineering began in Mr. Paul Pomperoy's AP Physics classroom. Without his dedication to teaching, and his commitment to ensuring that every one of his students

have a strong foundation in physics, I believe I really would have struggled in all of my engineering classes.

I am indebted to Lloyd Scarborough, who singlehandedly purchased, assembled, and installed nearly all of the equipment in the Mechatronics Research Lab. I simply would not have been able to build any of my hardware without this equipment. I appreciate the valuable advice and insightful suggestions that I received from Mike Robinson, Nick Kurczewski, and Kiron Mateti. I am also grateful for the comic relief that these same individuals as well as Taylor Blyth provided, especially during times when I was not sure I would ever be able to make all of my hardware work.

Lastly, I would like to thank my family for all their love and encouragement. For my parents who always encouraged me to do my best, in whatever endeavor I pursued, thank you.

# Nondestructive Forensic Pathology of Lead-Acid Batteries

## 1.1 Introduction

Lead-acid is the most widely used chemistry for batteries in stationary and hybrid applications, with the majority consisting of a valve-regulated lead-acid (VRLA) design. The most common damage mechanisms for a VRLA battery include corrosion of the positive electrode, irreversible hard sulphation on the negative electrode, water loss, degradation of the active material, electrolyte stratification, and short-circuits [1] [2] [3]. VRLA batteries are designed to minimize these effects as much as possible but the operating environment, cell-to-cell and battery-to-battery manufacturing variations, and use can cause different degradation mechanisms to dominate capacity loss and/or impedance rise. With accurate State of Health (SOH) monitoring, cell usage can be adjusted by the battery management system (BMS) to optimize the performance and life of the energy storage system. The BMS must be able to determine in real-time the predominant degradation mechanism for each cell and adjust use accordingly.

Gibson *et al.* [4] analyze sulfate formation inside lead-acid cells at low state-of-charge (SOC) using S.E.M and chemical means. Yamaguchi *et al.* [5] and Takehara [6] provided insight into

the formation and recrystallization of lead sulfate. Kim *et al.* [7] mathematically model corrosion layer growth and active mass loss inside a lead-acid cell. Cherif *et al.* [8] propose an aging model that includes the effects of deep discharge cycles associated with energy storage for photovoltaic systems. Lam *et al.* [9] demonstrate that high-current discharge is a key factor in causing lead-sulfate layer build-up during partial-state-of-charge operation. Schaeck *et al.* [10] [11] show that corrosion of the positive grid is the predominant degradation mechanism in micro-hybrid electric vehicles.

Most of the previous work on the aging of VRLA batteries focuses on a single cell or a single battery. Relatively few studies have investigated aging mechanisms in cells that are internally connected in parallel/series, the actual situation for most batteries and battery packs. The individual cell studies in the literature often use destructive techniques to establish the degradation mechanism. Piller *et al.* [12] summarized a list of nondestructive techniques for online state-of-charge estimation. Bhangu *et al.* [13] adopt a nonlinear observer to predict SOH of lead-acid batteries used in hybrid-electric vehicles. Gould *et al.* [14] and Fairweather *et al.* [15] propose two different approaches, subspace parameter estimation and pseudo random binary sequence excitation, to identify the parameters indicating the SOH of lead-acid batteries. Those techniques, however, do not specify or depend on degradation mechanisms that cause battery aging.

There are several experimental techniques that are nondestructive and elicit important information about a battery. SOH evaluation in the field on-board a vehicle requires nondestructive evaluation using as simple an algorithm as possible and the fewest number of sensors. This motivates the use of current and voltage data to assess battery health using full charge/discharge, pulse charge/discharge, and Electrochemical Impedance Spectroscopy (EIS). Huet [16] reviews impedance measurement techniques for SOC/SOH determination of secondary batteries. Viswanathan *et al.* [17] compare EIS tests on lead-acid batteries to show the effect of state of charge on the impedance spectrum. Mauracher *et al.* [18] identify the parameters of a dynamic model for a lead-acid battery using EIS measurements. Similarly, Buller *et al.* [19] develop

a non-linear equivalent circuit model of a lead-acid battery based on parameters from EIS testing. Thele *et al.* [20] study the gassing phenomenon for a lead-acid cell using EIS tests of the individual electrodes. Blanke *et al.* [21] give an overview of several impedance measurement-related approaches to assess SOC, SOH and cranking capability of lead-acid batteries in EVs/HEVs. EIS has also been widely used in studying of other battery chemistries. For instance, Hammouche *et al.* [22] and Bundy *et al.* [23] use EIS for SOC determination of Ni-MH batteries. Tröltzsch *et al.* [24] characterized the aging effects of lithium-ion batteries by using EIS. Yazami *et al.* [25], Bouchet *et al.* [26] and Abraham *et al.* [27] study the behavior of the electrodes during aging for different types of lithium-ion batteries.

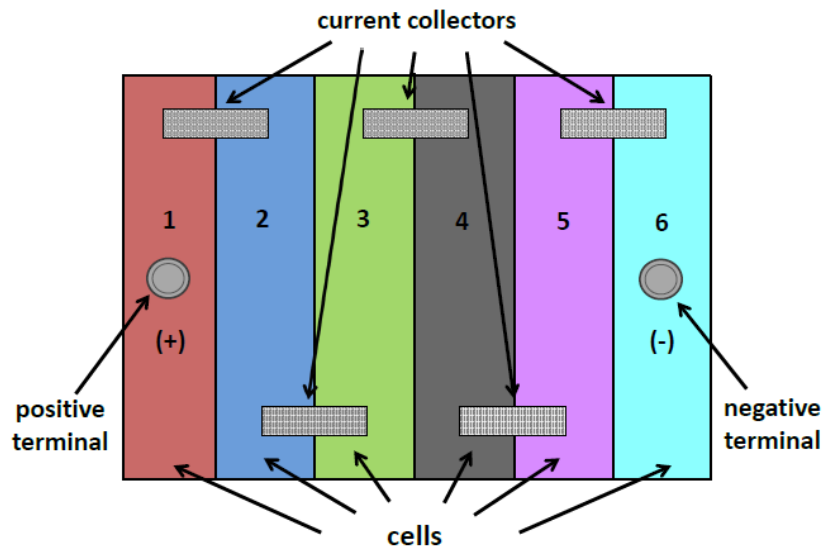


**Figure 1.1.** VRLA Battery Configuration: Six cells in chambers 1 - 6 are individually sealed and connected in series through current collectors.

In order for nondestructive forensic pathology of dead cells to work, each aging mechanism must have a unique signature that can be measured from the available sensors. In this work, individual cell voltage and pressure measurements are available and the current can be controlled to completely charge/discharge, pulse charge/discharge, and sinusoidally charge/discharge for EIS. These are considered to be nondestructive measurements because the access terminals and pressure ports could be built into the battery. Voltage and pressure sensors are attached during the autopsy to make the desired measurements. The results of this autopsy are then used to

revive the battery, adjust the BMS utilization, or direct recycling efforts.

In this study, a new 75Ah AGM VRLA battery is compared to a dead battery of the same make and model that was cycled over course of several months on an Arbin BT2000. Each battery consists of six chambers connected in series (see Fig. 1.1) containing eighteen cells in parallel. The test results are used to diagnose the dead chambers and their cause of the death. Since these cells in parallel were not differentiated in this study and their total voltage is the same as that of a single Pb-acid cell, they are referred as cells in this thesis.

## **1.2 Experimental Procedure**

### **1.2.1 Battery Cycling**

The dead battery was cycled on an Arbin BT2000 for 31,560 cycles using a duty cycle representative of an electric locomotive operating an 8 hour shift in a switchyard. The duty cycle consisted of 80 small pulse discharge/charge cycles and a constant-current-constant-voltage (CC-CV) charge at the end of the shift. The battery was declared dead when the capacity fell to approximately half of its initial value.

### **1.2.2 Full Charge/Discharge and Pulse Train Testing**

The new and dead batteries were fully charged and discharged using an AE Techron LVC 5050 linear amplifier controlled by dSPACE.

For pulse train testing, each battery was initially discharged to 70% SOC and then subjected to a charge-discharge cycle for 30 minutes. The pressure response was minimal during these tests so only the voltage data was collected.

The measured capacities of the new and dead batteries are 70-75Ah and 36-43Ah, respectively. During full charge/discharge testing, the batteries were discharged from 100% SOC until a cutoff voltage of 10V was reached. The batteries were rested for at least 24 hours and then charged

until a cutoff voltage of 15V was reached. Note that the current flowing through the new and dead batteries during testing were not equal, because of the noted difference in charge capacity.

Five rods were threaded to a depth of approximately 0.5 inches into the top of each cell current collector so that individual cell voltages could be measured during testing. Holes were drilled into each individual cell and tubes were inserted and sealed to enable pressure measurement (See Fig. 1.2). Omega PX309 pressure sensors were attached to the tubing and electrically connected to dSPACE to measure the cell pressures. All the cell pressures were zeroed so that the discrepancy in gas generation inside each cell is only due to the health condition of the cells.

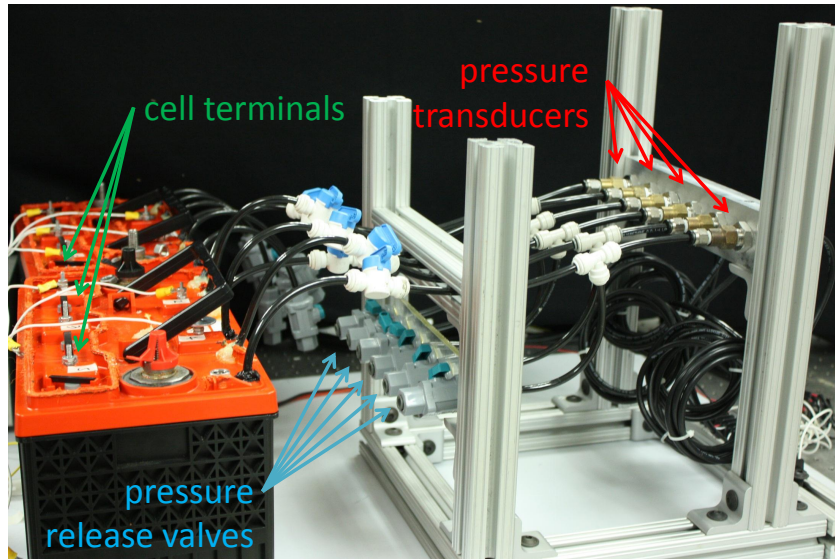


**Figure 1.2.** Photograph of the experimental setup.

### 1.2.3 Impedance Testing

Battery impedance was measured using the Frequency Response Analyzer (FRA) method, for which a small sinusoidal battery voltage and the current response are the input and output of the system, respectively [28]. The small cell voltage signal passes through an external circuit that removes the DC offset (i.e. the battery OCV) and amplifies the remaining AC signal. A DAQ system then reads the level-shifted and amplified voltage signal. The external circuitry ensures

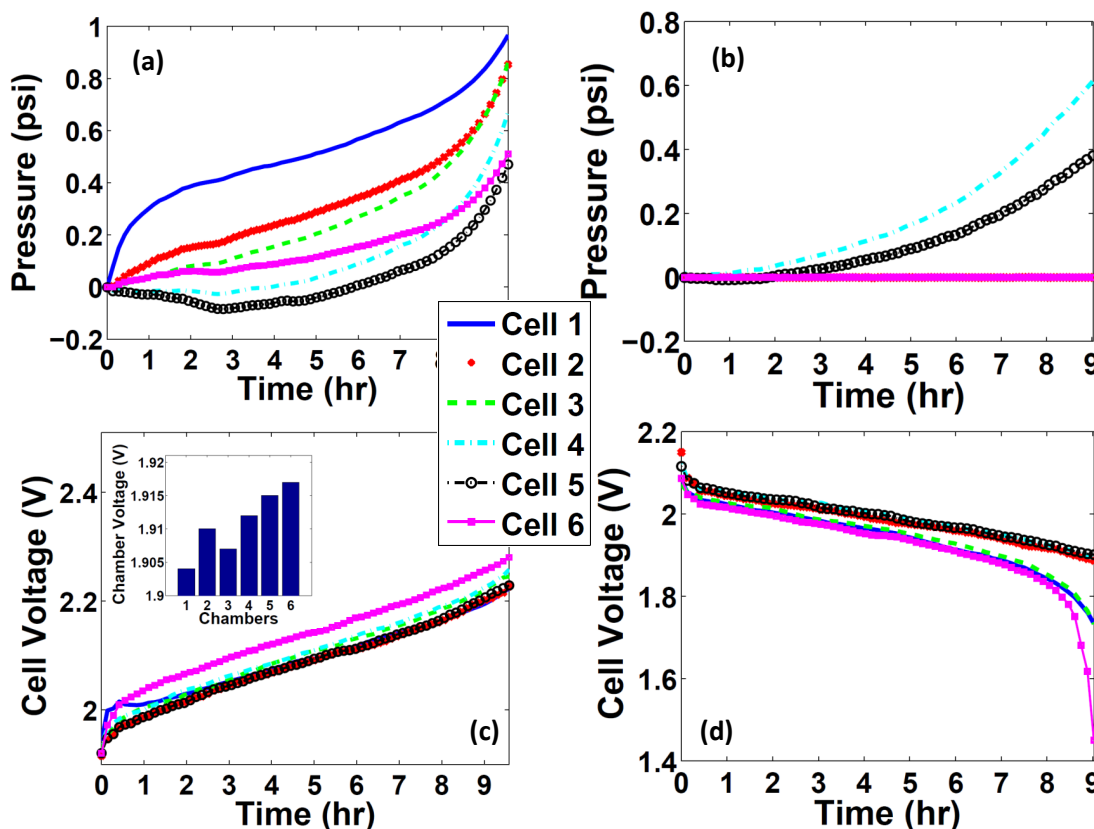


**Figure 1.3.** Charge/discharge of the new battery: (a) Cell pressure during charge; (b) Cell pressure during discharge; (c) Cell voltage during charge with inset showing initial distribution; and (d) Cell voltage during discharge with inset showing initial distribution.

that the voltage signal spans the full range of the analog to digital input channel. This reduces quantization error, which improves signal quality and reduces noise in EIS plots.

Since battery impedance is very small (on the order of  $m\Omega$ ), only a 10mV battery voltage signal was necessary for producing a substantial current response. The frequency of the battery voltage signal was held constant for five cycles at logarithmically spaced points between 0.01Hz to 100Hz. A FFT was used to analyze the voltage and current signals separately. Impedance was then calculated from amplitude and phase data. The test circuit was validated using a Solartron SI1255B Frequency Response Analyzer.

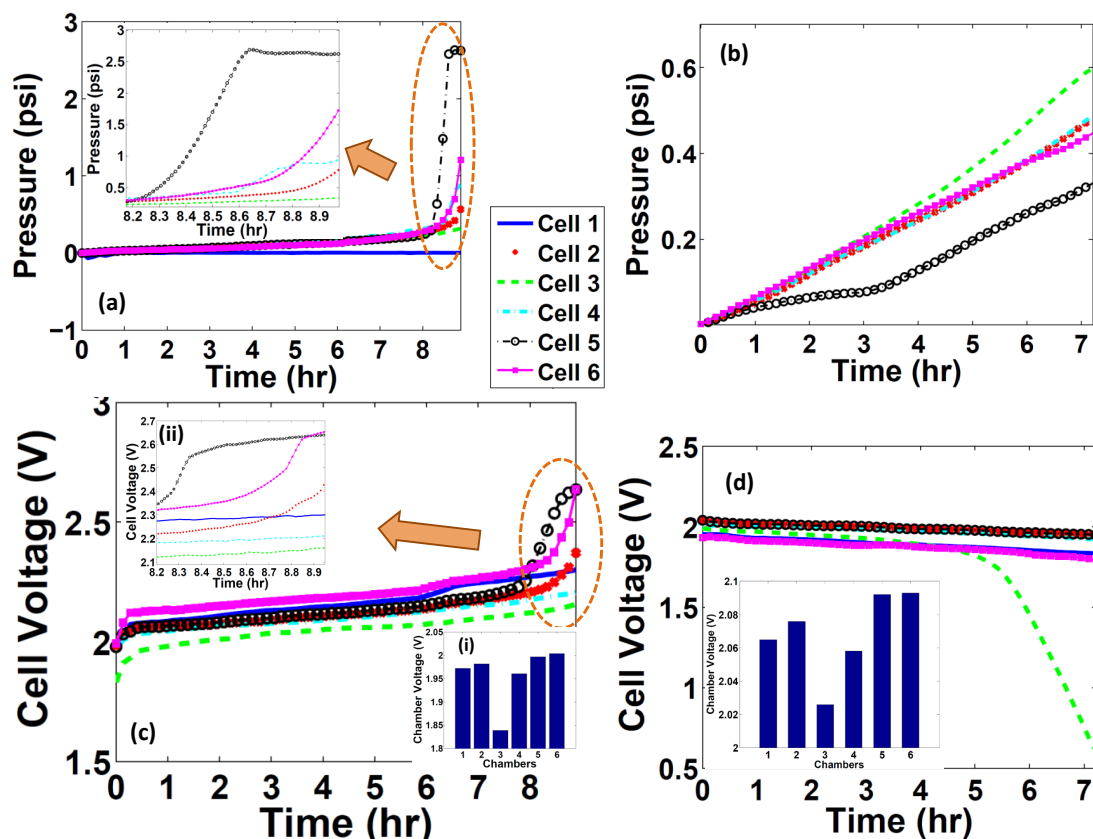


**Figure 1.4.** Charge/discharge of the dead battery: (a) Cell pressure during charge with inset showing pressure build-up; (b) Cell pressure during discharge; (c) Cell voltage during charge with inset showing initial distribution with inset (i) showing the initial distribution and (ii) showing voltage change at the end of charge; and (d) Cell voltage during discharge with inset showing initial distribution.

## 1.3 Results and Discussion

### 1.3.1 Full Charge/Discharge Testing

Figures 1.3 and 1.4 show the experimental results from full charge/discharge of the new and dead battery, respectively. The left column of each figure is for charge and the right column is for discharge. The charge starts from a fully discharged state at 12.5V and 11.5V for the new and dead batteries, respectively. The voltage immediately jumps at the onset of charge current due to the ohmic resistance and then slowly climbs to the cutoff voltage of 15V. Current rates of 7A and 5A for the new and dead batteries were chosen to be approximately  $C/10$ . The new and dead battery reach full charge after 10.2 hrs and 9.1 hrs, respectively, indicating charge rates

close to C/10. The total charge transferred to the new and dead batteries is 70Ah and 40Ah, respectively.

Other than the voltage shift due to increased ohmic resistance, the new and dead battery voltage curves look similar, especially at low state of charge (SOC). At higher SOC, however, the dead battery voltage curve loses the smooth quality of the new battery and has a nonuniform growth in slope.

The cause for this nonuniformity in the dead battery voltage curve becomes clear from the cell voltage and pressure measurements in Figs. 1.4(a) and 1.4(c), respectively. While there is almost no pressure generated in the new battery (See Fig. 1.3(a)), the dead battery shows significant pressure rise due to gassing in several cells. In fact, the inset of Fig. 1.4(a) shows the pressure in Cell 5 plateauing after 8.8 hrs, indicating that the cell vented excess pressure through a factory installed safety valve. The inset in Figure 1.4(c) shows that the growth in voltage is coordinated with the increase in pressure so the cells with demonstrated water loss (Cells 2, 5, 6) are directly responsible for the growth in voltage and associated reduction in capacity.

The hypothesis that water loss is responsible for the death of Cells 2, 5, and 6 is buttressed by the uneven voltage distribution in the cells prior to charge. Voltage is directly related to acid concentration [29] and acid concentration increases with water loss. The three cells with gassing also have the highest initial voltage as shown by the inset plot in Fig. 1.4(c). Contrast the uneven initial voltage distribution of the dead battery with the uniform distribution for the new battery in Fig. 1.3(c).

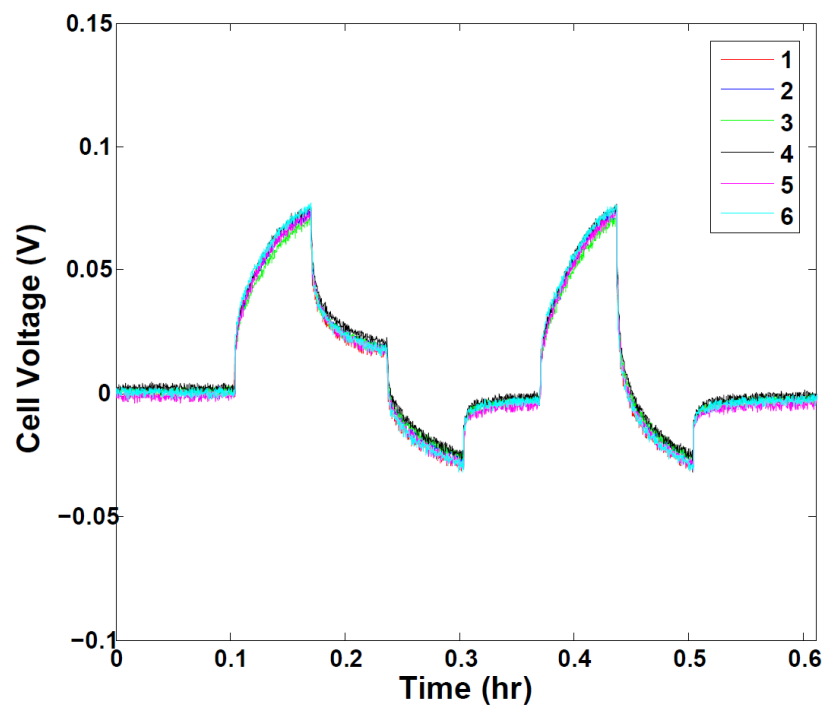
The discharge starts from a fully charged state at 12.61V and 12.41V for the new and dead batteries, respectively. The voltage immediately jumps at the onset of discharge current due to the ohmic resistance and then slowly decreases to the cutoff voltage of 9.5V. At the approximately C/10 current rate, the new and dead battery are fully discharged after 9.1 hrs and 7.2 hrs, respectively. The total charge delivered by the new and dead batteries is 70Ah and 40Ah, respectively.

In addition to the negative offset due to increased ohmic resistance, the dead battery discharge curve has a shorter plateau and more rapidly drops off with decreasing SOC. As expected, gassing does not play a significant role. The cell voltage plot in Fig. 1.4(d) shows that Cell 3 experiences a rapid decrease in voltage after five hours of discharge. The other five cells have relatively normal discharge curves and could provide significantly more charge if not for the reduction in battery voltage caused by Cell 3.

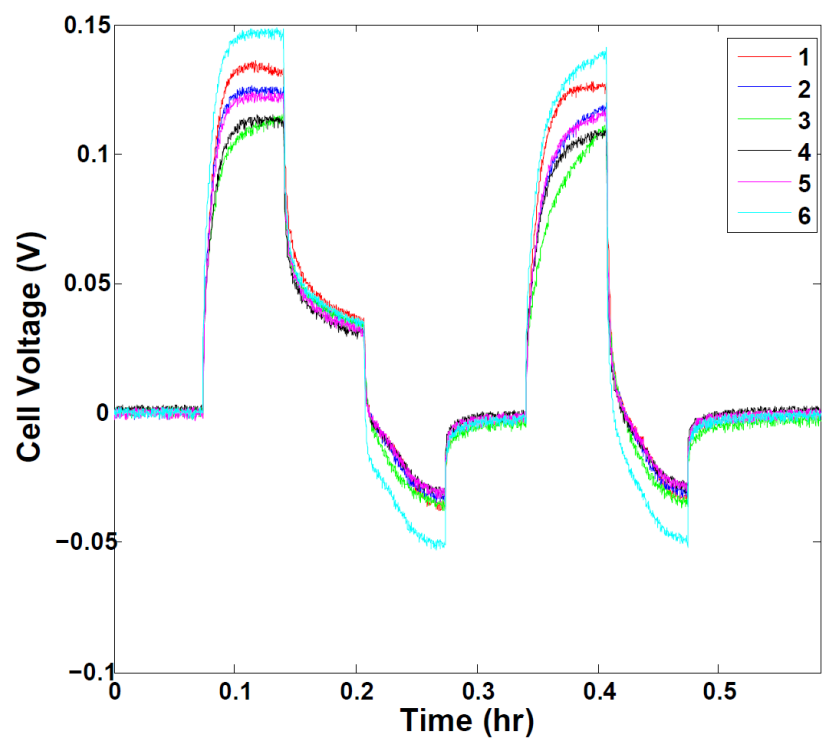
The rapid voltage drop in Cell 3 during discharge is indicative of sulphation. Sulphation reduces the effective active area and acid concentration, both of which decrease capacity. Cell 3 has the lowest initial voltage (see inset in Fig. 1.4(d)), indicating low acid concentration. Cell 3 also did not show symptoms of gassing during charge which would be indicative of corrosion, another possible degradation mechanism.

### 1.3.2 Pulse Train Testing

Figures 1.5(a) and 1.5(b) show the response of the new and aged batteries at 50% SOC to a current pulse train. The distribution of the new and aged cell voltages are dramatically different. The spread of voltages in the aged battery implies substantial differences in the states of health of each cell. Each cell of the new battery, on the other hand, shows a nearly identical dynamic response to the pulse train, suggesting that the variance in cell capacity and health is minimal. Figures 1.5(a) and 1.5(b) also show that the initial response of each cell (i.e. the large voltage jump at the start of the first current pulse) in the aged battery was much larger than the initial response of each cell in the new battery. This suggests that the aged battery has significantly larger ohmic resistance. Furthermore, the time constants of the cells within the aged battery vary considerably, which indicates differences in capacitance.



(a)



(b)

**Figure 1.5.** Pulse train voltage response of the new (a) and aged (b) batteries. The OCV of each cell was subtracted from each curve to facilitate comparisons between cells.

### 1.3.3 Impedance Testing

Figures 1.6(a) and 1.6(b) show the EIS results. Like the pulse train data, the distribution among the aged cells is much more spread out than that of the new cells. The individual cell EIS plots for the new battery are fairly uniform, showing the 45° tail at low frequency, a mid frequency arc associated with double layer capacitance, and high frequency inductance. The EIS plots of the aged battery are more distributed, showing widely ranging resistance and capacitance. Cell 6 of the aged battery exhibits the largest ohmic resistance, which agrees with the pulse train data; however, no other correlations based on resistance data can be drawn between the EIS and pulse train data.

The radius of curvature in the high frequency impedance region was measured to determine the relative capacitance of each cell in the aged battery. Table 1.1 lists the cells in order of increasing capacitance, with 1 corresponding to the cell with the smallest capacitance and 6 to the largest (capacitance is inversely proportional to impedance).

Besides the increase in overall resistance due to aging, the correlation between the observed EIS spectra and specific degradation mechanisms is unclear, however, and warrants further study.

**Table 1.1.** The radius of curvature of each cell within the aged battery.

Cell	Red	Blue	Green	Black	Maroon	Cyan
Radii ( $m\Omega$ )	0.7591	0.7693	0.7985	0.8858	0.6459	0.6892
Ranking	4	3	2	1	6	5

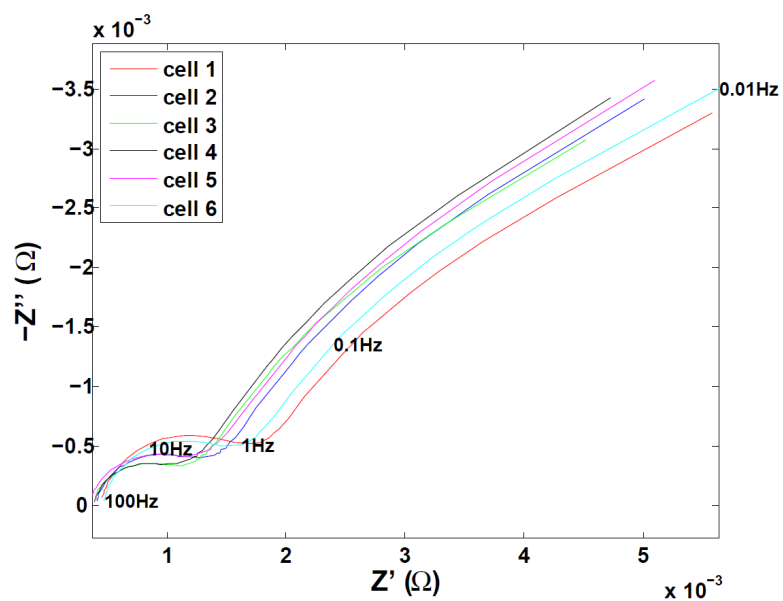
## 1.4 Conclusions

The cause of death for VRLA batteries can be determined from a full charge/discharge cycle while monitoring individual cell pressures and voltages. In this study, Cells 2, 5, and 6 of a dead VRLA battery became overcharged and started gassing earlier than other cells during charge so the cause of death for these cells was dehydration. Cell 3 displayed a sharp, voltage drop during

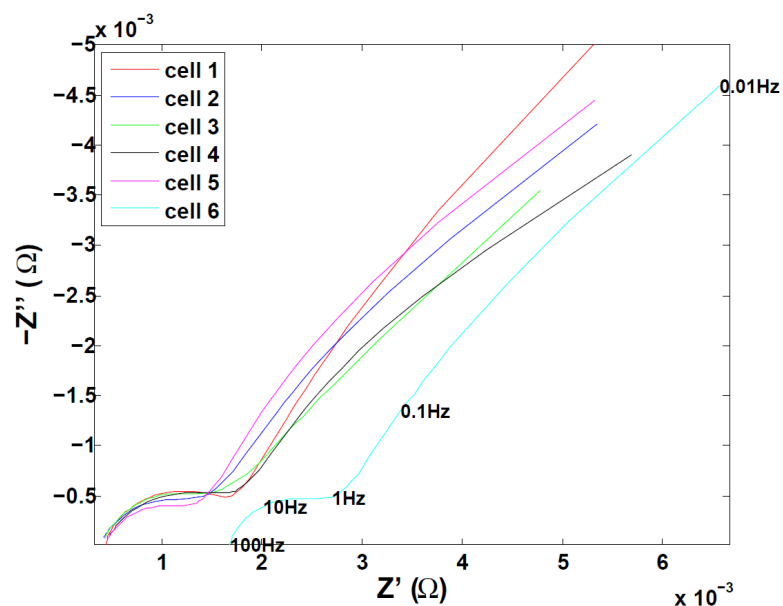
discharge, indicating death by sulphation.

The pressure rise associated with gassing was accompanied by a sharp rise in cell voltages. This suggests that individual cell pressure sensors equipment might not be necessary to observe gassing.

The pathological capabilities of EIS and short duration pulse charge/discharge is not clear. The pulse train response and EIS curves are different for the dead and new batteries and cells but the correlations are not fully understood. On-board SOH monitoring is more practical if the real-time data from everyday use can be used to determine the battery capacity. This motivates further study into the predictive capability of pulse train and EIS testing.



(a)



(b)

Figure 1.6. EIS plots of the new (a) and aged (b) batteries from 0.01Hz to 100Hz.

# Appendix **A**

## Battery Testing Hardware

There are currently no commercially-available, off-the-shelf products that are capable of performing a wide range of battery tests. Arbin machines, for example, are capable of charging or discharging batteries at very large currents, but they can only be programmed to conduct cycling, pulse train tests, or some variation of the two. Other equipment can measure battery impedance, but like the Arbin, these machines are only designed to perform a single function.

A programmable battery testing machine (PBTM) was designed to incorporate the capabilities of various battery testing machines into a single piece of hardware. The PBTM is capable of charging or discharging a 12V lead-acid battery at up to +/-20A. It can be programmed to conduct standard battery tests, such as cycling or pulse train tests. It can also measure impedance and can produce EIS plots. The PBTM even has the ability to conduct more sophisticated tests that require atypical battery controllers, like battery desulfation for example, which uses pressure feedback to control current. The principal advantage of the PBTM, therefore, is its flexibility to perform essentially any type of battery test the end user desires. The following sections describe how the PBTM was designed and how it operates.



**Figure A.1.** The PBTM is shown below the amplifier and above the DAQ system.

## A.1 Power Supplies and Grounding

### A.1.1 Power Supplies

The PBTM is designed to minimize the amount of noise in current and voltage measurements. High-fidelity, noise-free signals are required for impedance measurements, among other things. Power supplies play a crucial roll in the design of circuitry that aims to minimize noise in measurement signals. Noise that is present in the power supply rails of an op-amp, for example, will ultimately appear in the op-amp's output signal. The same principle applies to current sensors as well: any noise present in the sensor's power supply lines will work its way through the internal measurement circuitry and reappear in the output signal. Therefore, one of the keys to reducing noise in measurement signals is to ensure that the power supply itself is not producing

much noise.

Simple AC to DC rectification circuits, like the one shown in Figure A.2, produce extremely quiet output voltage signals. These circuits are much less noisy than switching power supplies, for example, because they use linear voltage regulators. Voltage regulators eliminate the need for many of the electrical components found in a switching power supply, which results in less electro-magnetic interference. The disadvantage of voltage regulators is that they are limited by the amount of current that they can source, which is typically between 1A to 1.5A. Switching power supplies, on the other hand, are capable of sourcing much more current.

The power supply shown in Figure A.2 would not be able to source enough current to power all of the loads (i.e. fans, power relays, reed relays, and integrated circuits) within the PBTM; however, the op-amps and current sensors are the only components that require highly regulated, quiet voltage supplies. Therefore, the voltage regulators are used solely to power the op-amps and current sensors. A 12V switching power supply, shown in figure A.3, provides current to the fans and relays, whose performance is not affected by any noise in the voltage supply lines.

Figure A.2 shows 5 voltage rails: +5V, +12V, -12V, +18V,-18V. The +5V rail is used to powers the current sensor and the +/-12V and +/-18V provide power to the op-amps. The need for two different sets of op-amp rail voltages is explained in SectionA.2.2.

### A.1.2 Grounding

Separating current conducting and signal grounds is another way to reduce noise. For this reason, great care was taken to avoid connecting the amplifier and data acquisition system (DAQ) grounds together. Figure A.4 shows that the input signal to the amplifier uses its own independent DAQ ground lead (blue wire) and is not connected to the amplifier output signal ground (green wire). Connecting the input and output ground leads creates ground loops, which cause hum and noise problems in the amplifier output [30]. Furthermore, large current flowing through the DAQ ground creates noise and measurement inaccuracy in ADC input channels. Only a small current,

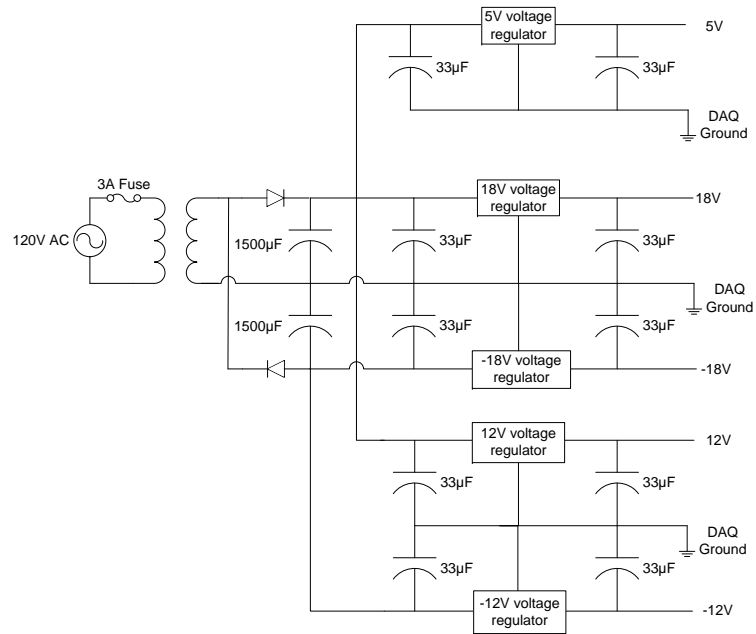
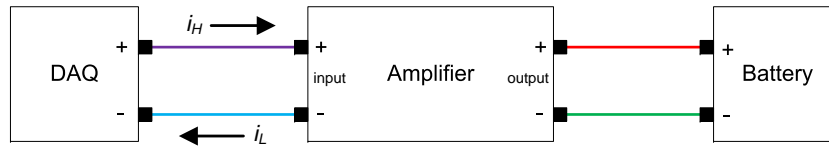


Figure A.2. PCB Power supply



Figure A.3. SL Power GECA20-12G 12V Power supply



**Figure A.4.** The DAQ ground lead (blue wire) is not connected to the amplifier output signal ground (green wire) to avoid hum and noise problems. Ground isolation also ensures that the current flowing into the low side of the ADC input channel is equal to the current flowing out of the high side, i.e.  $i_L = i_H$ .

equal in magnitude to that flowing into the low side (ground) of the input channel should flow through the high side of the ADC input channels.

To avoid another possible source of ground loops, the metal casing that houses the PBTM is not directly connected to the earth ground. Typically any electrical equipment housed within a metal case is grounded to the third wire (earth ground) of an AC mains connection. Since the case of the amplifier is already grounded and in contact with the PBTM casing, any additional grounding is unnecessary and might cause ground loops.

As mentioned in section A.1.1, a 12V switching power supply powers the fans and relays. The negative terminal of the power supply is floating in much the same way that the negative terminal of a battery is floating. The floating 12V supply prevents the low-side NPN transistors, which switch the relays on and off, from working correctly. For the transistors to function properly, the 12V signal that is used to power the relays must be grounded. In other words, although 48V and 36V signals will power the relays without a problem, the transistors will not work because the transistor base signal is a 5V signal relative to the DAQ ground (see section A.4 for further detail). Therefore, the negative terminal of the power supply is connected to the earth ground to ensure that the transistors work correctly. The earth ground, rather than the DAQ ground, is used to ground the power supply to prevent any significant amount of current from flowing into the DAQ ground. Furthermore, ground isolation is always good practice because it minimizes the possible sources of noise in measurement signals.

## A.2 Voltage Measurement

### A.2.1 Amplifier Voltage Measurement

The previous section highlighted the benefits of separating the amplifier ground from the DAQ ground. One disadvantage of ground separation is that measuring amplifier voltage becomes slightly more complicated. To avoid connecting the DAQ and amplifier grounds, amplifier voltage,  $V_{amp}$ , must be indirectly measured. Figure A.5 shows the two voltage measurements that are needed to find amplifier voltage: (1) the positive amplifier output relative to the DAQ ground,  $V_{amp(+)/DAQ}$ , and (2) the negative amplifier output relative to the DAQ ground  $V_{amp(-)/DAQ}$ . An inverting op-amp scales down the positive amplifier signal so that it does not exceed the +/-10V voltage limit of the ADC input channel. The negative amplifier signal,  $V_{amp(-)/DAQ}$ , is then subtracted from  $V_{amp(+)/DAQ}$  to obtain the amplifier voltage,  $V_{amp}$ .

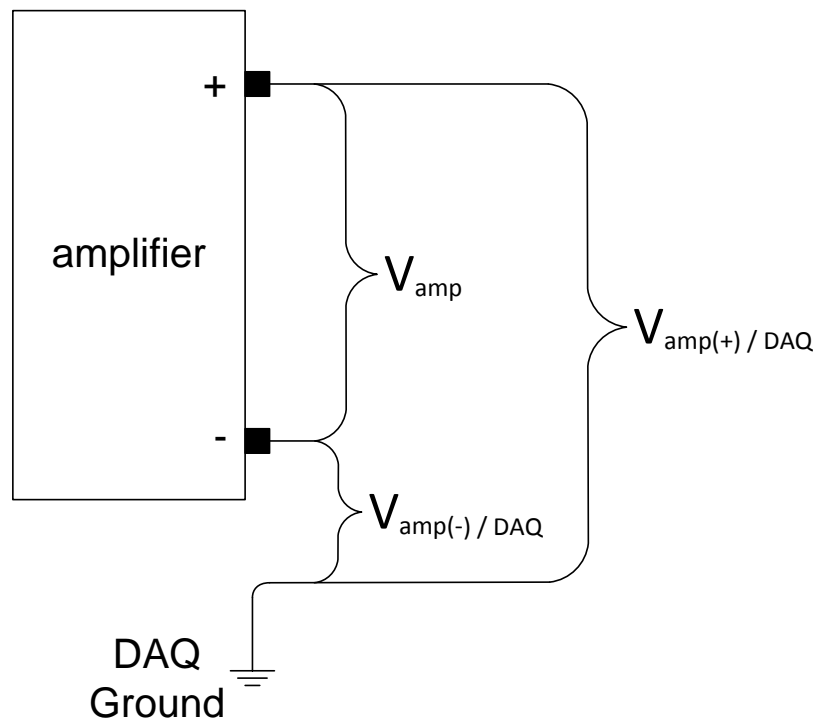


**Figure A.5.** Amplifier voltage is measured by taking the difference between  $V_{amp(+)/DAQ}$  and  $V_{amp(-)/DAQ}$ .

A double-pole, single-throw (DPST) reed relay controls the gain of the op-amp that is used to scale down amplifier voltage. Figure A.6 shows that a reed relay connects one of two feedback resistors,  $R_{f_1} = 20k\Omega$  or  $R_{f_2} = 10k\Omega$ , to the output of the op-amp. With a fixed input resistance of  $R_{in} = 40k\Omega$ , the gain of the op-amp can be toggled between  $G = 0.5$  or  $G = 0.25$ . Given the measuring range of the ADC input channels and the possible gains of the op-amp, the circuit is capable of measuring voltages up to  $20V$  or  $40V$ , depending on the gain selected.

The ability to switch between two measuring ranges is useful for several reasons. If a large measuring range is not required for a certain type of test, the low range (i.e.  $G = 0.5$ ) signal can be used. The smaller scaling factor means that a larger voltage will be read by the ADC input channel. The larger signal will be more accurate and less noisy since it will use a greater portion of the ADC measuring range. A quieter signal will afford better feedback control and will reduce the amount of noise in the amplifier output signal.

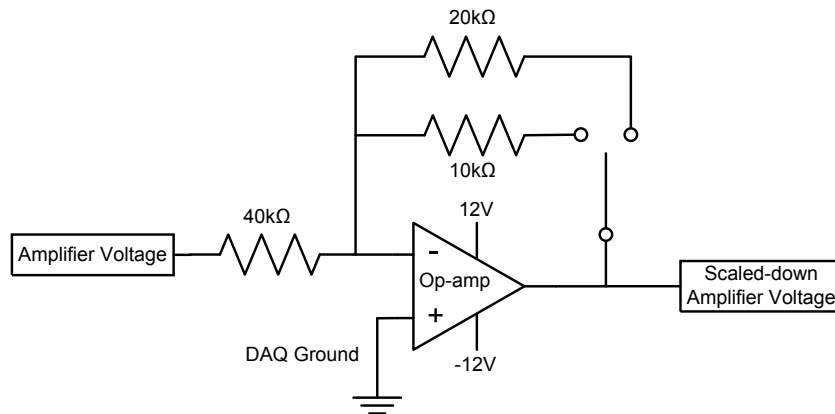


**Figure A.6.** Op-amp with adjustable gain used to measure amplifier voltage.

## A.2.2 Battery and Cell Voltage Measurement

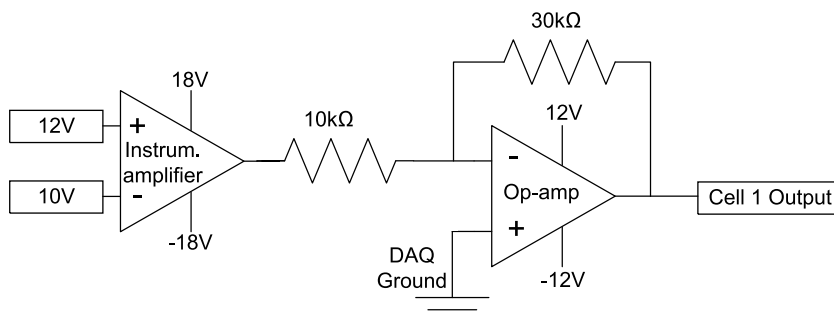
Battery voltage is calculated by summing all 6 cell voltage measurements. Measuring cell voltage, however, is not as straightforward as one might expect. The following paragraphs explain the difficulty in using conventional methods to measure cell voltage and how these challenges were

solved.

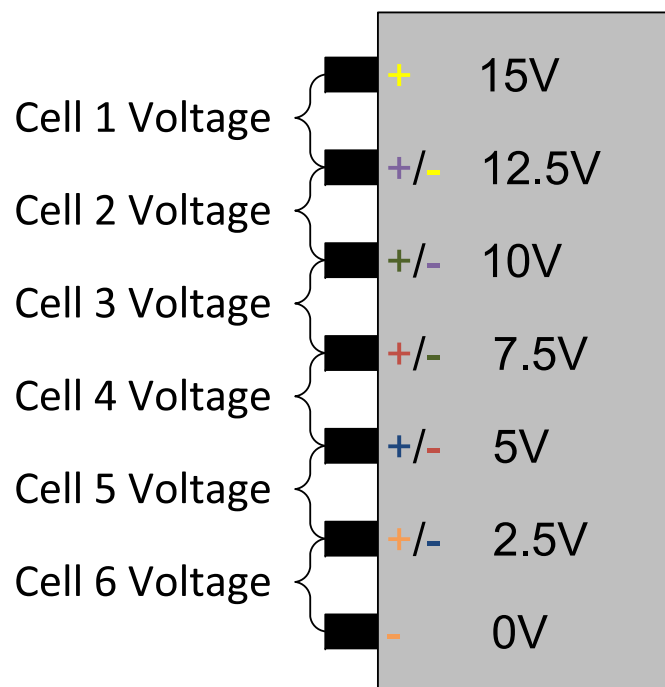
The negative terminal of the battery is connected to the amplifier ground. Since the amplifier and DAQ grounds are approximately equal, the negative battery terminal can be considered to be approximately the same voltage as the DAQ ground. This means that voltages of the positive and negative electrodes of cell 3, for example, are approximately 8V and 6V, with respect to the DAQ ground. The positive lead of the ADC input channel could be connected to the 8V terminal; however, connecting the negative lead of the ADC channel to the 6V terminal will create a short, since the negative lead is held at a constant voltage of 0V. Therefore, cell voltages cannot be directly measured with a single ADC input channel. Two individual ADC input channels, however, could be used to separately measure the 8V and 6V terminal voltages. The difference could then be calculated to find cell voltage. This measurement method, although perfectly acceptable for measuring cell voltage under normal circumstances, does not work well for measuring cell voltage during impedance measurements (this is explained in further detail in section A.7.2). An entirely different, yet equally viable approach to measuring cell voltage uses instrumentation op-amps, which are highly accurate difference amplifiers.

Figure A.7 shows how instrumentation amplifiers measure cell voltage. For a given cell, the lower potential electrode voltage is subtracted from the higher potential electrode voltage, and the difference (i.e. the cell voltage) is output relative to the DAQ ground. The instrumentation amplifiers that measure the voltages of cell 1 and cell 2 use +/-18V supply rails. The other cells are measured with instrumentation amplifiers that use +/-12V supply rails. The reason for this difference is explained in the following paragraph.

Both input signals of an instrumentation amplifier must fall between the voltage rails. In other words, an instrumentation op-amp with +/-12V supply rails cannot measure the voltage difference between a 100V and 98V signal. Even though the difference between these signals, a mere 2V, is well within the range of the supply rails, the input signal voltages (100V and 98V) are not. Figure A.8 shows the maximum possible voltage of each electrode relative to



**Figure A.7.** Circuit used to measure cell voltage.



**Figure A.8.** The maximum voltage of each electrode relative to the negative battery terminal.

the negative terminal of the battery. Both electrodes of cell 1 and the positive electrode of cell 2 clearly exceed 12V. Therefore, the  $\pm 12V$  supply rails would not be adequate for the instrumentation amplifiers used to measure the voltages of cell 1 and cell 2. For this reason,  $\pm 18V$  supply rails are used to power the instrumentation amplifiers that measure the voltages of cell 1 and cell 2.

The instrumentation op-amps with  $\pm 18\text{V}$  supply rails could damage the data acquisition system since the ADC input channels of the DAQ system can be permanently damaged by voltages in excess of  $\pm 15\text{V}$ . Under normal circumstances, the output signal of the instrumentation op-amps will vary between 1.7 to 2.5V, which is not even close to exceeding the  $\pm 15\text{V}$  ADC limit; however, op-amps will output a rail voltage if they become saturated or if they are not connected properly. If the negative voltage supply connection is loose and disconnects, for example, an op-amp will output its positive rail voltage. If this were to happen to one of the instrumentation op-amps with  $\pm 18\text{V}$  rails, the op-amp would output 18V and damage the DAQ.

To prevent damage to the DAQ system, an inverting op-amp with  $\pm 12\text{V}$  supply rails is placed between the instrumentation op-amp with  $\pm 18\text{V}$  supply rails and the ADC input channel (see figure A.7). The inverting op-amp ensures that the highest voltages the ADC channel will see are  $\pm 12\text{V}$ , regardless of the voltage at the input of the inverting op-amp. Aside from providing overvoltage protection, the inverting op-amp also serves to amplify the cell voltage by a gain of  $G = 3$ . Since cell voltage will never be much greater than 2.5V, amplifying the signal will allow for a much greater portion of the range of the ADC input channel to be utilized.

## A.3 Sensors

### A.3.1 Current Sensor

Two LEM CASR-6NP hall-effect transducers measure current. A “high-range” and “low-range” sensor are capable of measuring currents up to  $\pm 20\text{A}$  RMS and  $\pm 6.7\text{A}$  RMS, respectively. Although both sensors are identical, the current conducting pins of the low-range transducer are connected so that the primary signal loops through the sensor three times. This decreases the sensor’s measuring range, but increases the sensitivity of the transducer by a factor of three. Increasing sensitivity is advantageous for the following reason: the secondary voltage signal of the CASR-6NP contains inherent noise that is constant at all current levels and even present when the

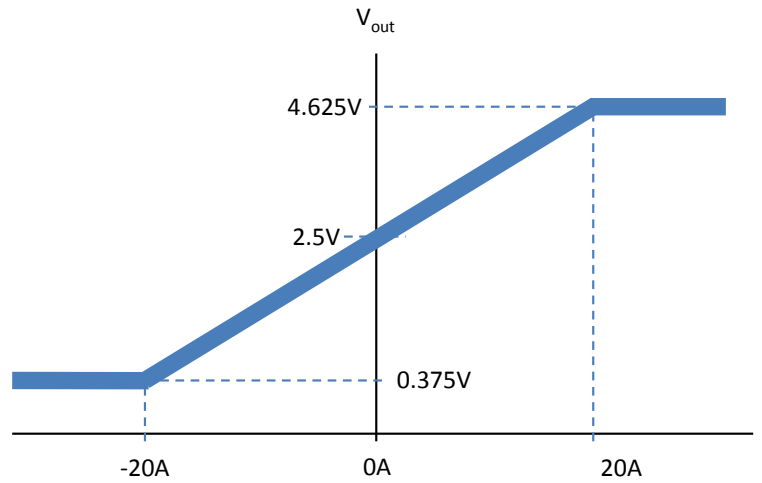


**Figure A.9.** Current sensor voltage output vs sensed current

sensor is not measuring any current. For a given current, greater transducer sensitivity increases the magnitude of the secondary signal, yet the level of inherit noise remains the same. Therefore, increasing sensitivity improves the signal to noise ratio (SNR) of the sensor.

A DPST power relay switches between the high and low-range current sensors. Therefore, current never flows through both sensors at the same time. The desired sensor is always selected before the amplifier is connected to the battery. Switching between the current sensors while current is flowing through the battery will momentarily open the circuit, which will create a large disturbance for the constant current (or constant voltage) controller.

The CASR-6NP outputs a secondary voltage signal that is proportional to the magnitude of the current being sensed. Figure A.9 shows that the output signal swings between 0.375V and 4.625V for the minimum and maximum current values that the transducer is capable of sensing, respectively, and is approximately 2.5V for 0A. The output signal is measured relative to a reference voltage, which hovers around 2.5V as well.

The output signal spans a range of only 4.25V, which is only about a fifth of the full 20V

range of any DAQ ADC input channel. To use a much greater portion of the channel's range, a Texas Instruments INA114AP instrumentation amplifier subtracts the reference signal from the output signal and amplifies the difference by a factor of three. Since the gain of this particular instrumentation amplifier is defined by the equation  $G = 1 + \frac{50k\Omega}{R_G}$ , a  $20k\Omega$  resistor is used to achieve a gain of  $G = 3.5$ . Using a greater portion of the input channel range decreases quantization error and increases the Signal-to-quantization-noise ratio. The accuracy of the current sensor is further improved by removing the offset error in software before conducting any tests. As a result, the gain error is the only significant source of sensor inaccuracy at room temperature.

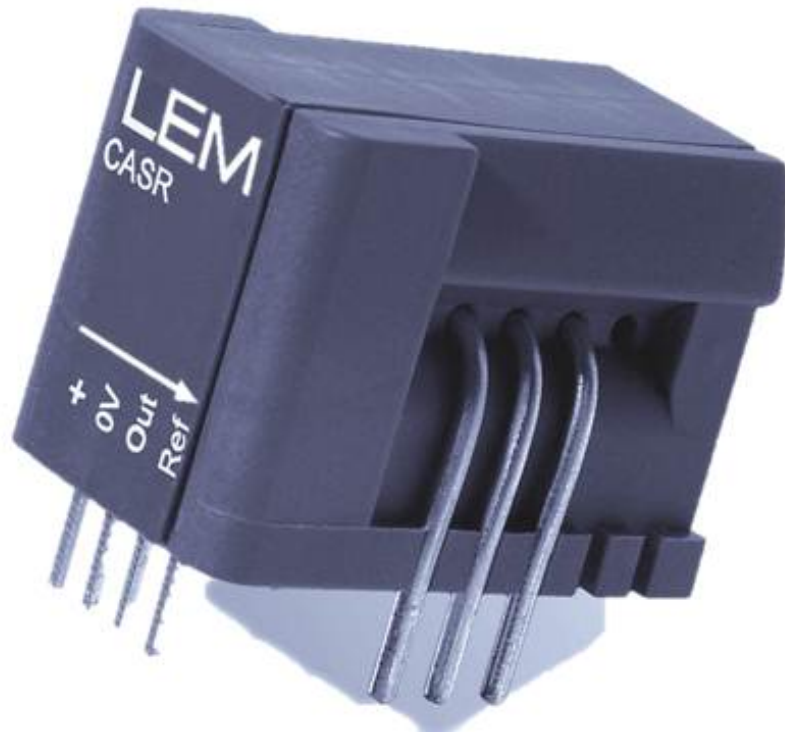


**Figure A.10.** A CASR 6-NP current sensor.

### A.3.2 Pressure and Temperature Sensors

Omegas PX309 Series pressure transducers measure the guage of each of six chambers of the lead-acid battery. These transducers are capable of measuring guage pressures ranging from 0 to 5 psi with 0.25% accuracy. Before recording data, the offset error of each guage pressure transducer is removed in software. An additional absolute pressure transducer measures atmospheric temperature. The atmospheric and guage pressure signals are summed to measure absolute pressure. A National Semiconductor LM34 measures room temperature.

## A.4 Relays

Power relays switch between different sets of resistors during charging and discharging. During EIS testing, the relays disconnect all power resistors from the circuit so that the battery and amplifier are directly connected. Therefore, the only resistance present is due from the wire itself. Small signal, DPST reed relays are used on the PCB to switch output signals between different input sources. Both the power relays and reed relays are actuated using NPN low side switches. TTL output signals are connected to the transistor bases.  $100\Omega$  resistors draw a sufficient amount of current to force the transistors into saturation.

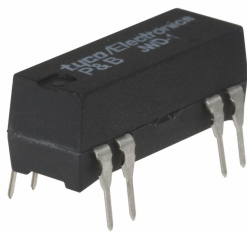


**Figure A.11.** A Potter & Brumfield JWD-172-161 DPST reed relay.



**Figure A.12.** A Panasonic HG2-DC12V-F DPDT 20A power relay.

Flyback diodes are connected across the power resistors coils to prevent voltage spikes as the magnetic field in the coil collapses. The reed relays contain internal flyback diodes.

#### A.4.1 Battery-Amplifier “Handshake”

A relay connects the battery to the amplifier. Before actuating the relay to close the circuit, the amplifier voltage is set to the open circuit voltage (OCV) of the battery or cell. If the amplifier voltage and voltage of the battery or cell are approximately equal, no significant amount of current flows when the relay completes the circuit.

### A.5 Battery Charging and Discharging

Although a linear amplifier is an ideal power source for frequency response testing like EIS, amplifiers are not designed to source or sink the large DC currents associated with battery cycling. DC signals only pass through half of the available internal heat sinks within an AC amplifier. As a result, current and voltage ratings for amplifiers must be derated by a factor of 2. Typically, battery cycling is conducted using a programmable DC power supply for charging and a variable load for discharging. To avoid using three separate pieces of equipment (i.e. amplifier, power supply, and variable load), an external circuit consisting of power resistors and relays was designed to ensure that an AE Techron LVC 5050 Linear Amplifier could charge and discharge a 12V lead-acid battery at up to +/-20A continuously. Additionally, amplifier settings were configured to maximize current capacity and minimize internal heat generation.

Although it may be counterintuitive, very low voltage signals create more heat within the amplifier than higher voltage signals. A basic understanding of how the amplifier works is necessary to explain this behavior. The LVC 5050 has two internal voltage rails. The positive and negative voltage rails maintain constant voltages of +90V and -90V, respectively. Transistors scale down the rail voltages to the desired output levels and dissipate the remaining voltage as heat. A desired amplifier voltage of 30V, for example, would require the positive rail transistor to dissipate 60V as heat. In other words, there is a larger voltage drop within the amplifier than across the load itself. Commanding the amplifier to source large amounts of current at very low

voltage levels, therefore, produces an excessive amount of heat that can damage the amplifier. To avoid this scenario, external power resistors increase amplifier voltage during high-current charging and draw current away from the amplifier during high-current discharging.

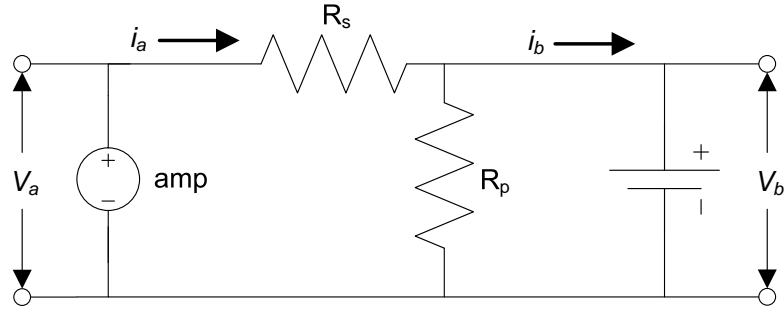


**Figure A.13.** Resistors are connected in series and in parallel with the amplifier. Battery current,  $i_b$ , is positive when the battery is being charged and negative when the battery is being discharged. Amplifier current,  $i_a$ , is positive when the amplifier is sourcing current and negative when the amplifier is sinking current.

For the circuit shown in Figure A.13, amplifier voltage and current can be derived using Kirchhoff's circuit laws. These relations (equations A.1 and A.2) are expressed as functions of battery current.

$$V_a(i_b) = R_s i_b + \left(1 + \frac{R_s}{R_p}\right) V_b \quad (\text{A.1})$$

$$i_a(i_b) = i_b + \frac{V_b}{R_p} \quad (\text{A.2})$$

### A.5.1 Discharging

During battery discharge, a resistor is connected in parallel with the circuit to reduce the amount of current that the amplifier sinks. Equation A.2 shows that the slope of  $i_a(i_b)$  is fixed at 1, but that the y-intercept can be moved by varying the value of  $R_p$ . Figure A.14 visually demonstrates this concept as well. If no parallel resistor is present,  $R_p = \infty$  and the y-intercept of Equation A.2 approaches zero. In this case, amplifier and battery current are equal. In other words, the

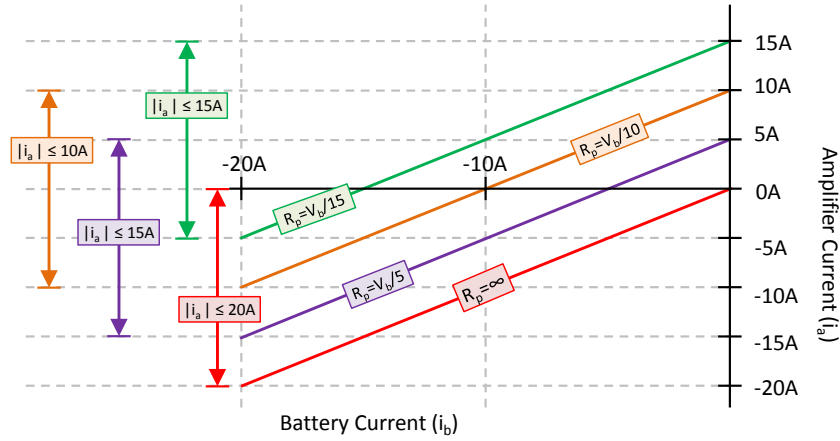


**Figure A.14.** Amplifier current,  $i_a$ , as a function of battery current,  $i_b$ , for different values of parallel resistance,  $R_p$ . The red curve represents  $i_a(i_b)$  if no parallel resistor is included in the circuit (i.e. infinite parallel resistance). As  $R_p$  decreases and the the y-intercept of the curve  $i_a(i_b) = i_b + \frac{V_b}{R_p}$  increases from zero, the maximum amount of current that the amplifier must sink or source decreases until reaching a minimum and then begins to increase. The orange curve,  $i_a(i_b) = i_b + 10$ , represents the case where the maximum amount of current that the amplifier must sink or source (i.e.  $|i_a|$ ) is minimized.

amplifier must sink all of the current that the battery is discharging, which can be as much as 20A. If the value of  $R_p$  is specified such that  $\frac{V_b}{R_p} = 10$ , the amplifier will only need to source or sink a maximum of 10A for  $-20 \leq i_b \leq 0$ . Therefore, adding a resistor in parallel can reduce the amount of current the amplifier sinks by as much as 50%.

After selecting an optimal value of  $R_p$  that minimizes the magnitude of amplifier current, the series resistance,  $R_s$ , can be specified. Equations A.1 and A.2 show that  $R_s$  does not influence amplifier current, but does affect amplifier voltage. Therefore, a value of  $R_s$  can be chosen to shape the amplifier voltage curve to one's liking. Ideally, amplifier voltage should be zero at the same point that the amplifier current is zero, as demonstrated in Figure A.15. In other words, the x-intercepts of the  $i_a(i_b)$  and  $V_a(i_b)$  should be equal. The reasoning for this requirement is as follows:

As described in a previous section, the amplifier can be damaged if it sinks or sources large currents at low voltages. Thus, there are two separate conditions that generate a significant amount of heat within the amplifier: (1) high currents and (2) low voltages. The amplifier

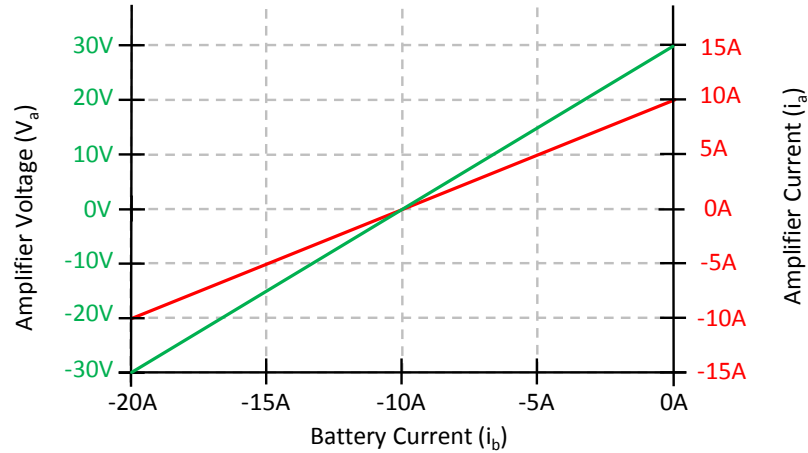


**Figure A.15.** Ideally amplifier current and voltage should intersect their respective x axes at the same battery current. In other words, amplifier voltage should be zero at the same point that amplifier current is zero.

voltage curve can be shaped (with an appropriate value of  $R_s$ ) such that these two conditions never coincide. For this reason, amplifier voltage should be minimized at low currents and should increase as current increases. In others words, the x-intercepts of the equations A.1 and A.2 should be as close as possible.

The x-intercepts of  $i_a(i_b)$  is already fixed at -10 by the value of  $R_p$  that reduces amplifier current by 50%. Therefore,  $V_a(i_b)$  should cross the x-axis as close to -10 as possible. The x intercept of  $V_a(i_b)$  is defined by equation A.3.

$$i_{b_x} = -\frac{V_b}{R_p} - \frac{V_b}{R_s} = -10 - \frac{V_b}{R_s} \quad (\text{A.3})$$

Equation A.3 shows that placing the x-intercept at -10A requires a infinitely large  $R_s$ . Although a large value of  $R_s$  will allow  $i_{b_x}$  to approach -10A, a large  $R_s$  will also cause amplifier voltage to increase rapidly since the value of  $R_s$  affects the slope of equation A.1. Therefore, after ensuring that adequate consideration is given to the voltage and power limitations of the amplifier, that value of  $R_s$  should be made as large as possible so that  $i_{b_x}$  is as close to -10A as possible.

Depending on whether the whole or a single cell is being charged or discharged,  $V_b = 12V$  or

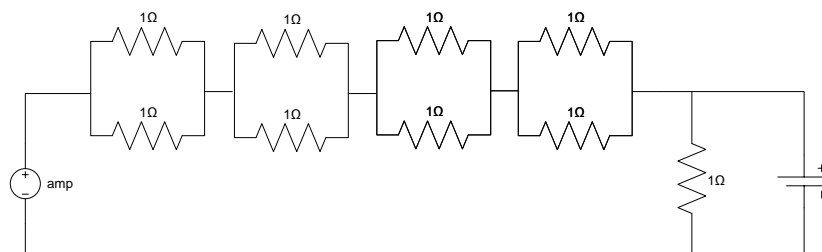


**Figure A.16.** A total of  $2\Omega$  is connected in series with battery. A  $1\Omega$  resistor is connected in parallel as well.

$V_b = 2V$ , respectively. Given these values, the ideal parallel and series resistances for charging a whole battery are  $R_p = 1.2\Omega$  and  $R_s = 3\Omega$ . For charging an individual cell, ideal resistances are  $R_p = .2\Omega$  and  $R_s = 3\Omega$ . These resistances were determined using the design guidelines detailed in the preceding paragraphs.

The actual hardware uses a  $1\Omega$  resistor in parallel and a  $2\Omega$  resistor in series during discharge. These resistances are used for both a single cell and the whole battery. The ideal resistance values were not used because the thorough analysis described above was not available at the time of assembly; nonetheless, the current hardware seems to be working satisfactorily during discharge.

Figure A.16 shows four sets of 100W  $1\Omega$  ceramic power resistors connected in series with the battery. Each set consists of two resistors connected in parallel. Since each set has an equivalent resistance of  $0.5\Omega$ , the total equivalent resistance connected in series with the battery is  $2\Omega$ . A 250W  $1\Omega$  ceramic power resistor is connected in parallel with the battery and amplifier before the series resistance.

## A.5.2 Charging

Adding resistance in series with the battery during charging increases the amplifier output voltage, which as described previously, decreases heat dissipation. There is no benefit to adding a resistor in parallel during charging. Equation A.2 shows that any resistance connected in parallel with the amplifier will require the amplifier current to exceed the battery current. In other

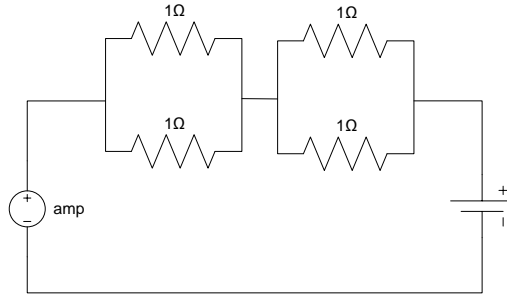


**Figure A.17.** A total of  $1\Omega$  is connected in series with battery.

words, a parallel resistor only forces the amplifier to source more current than would otherwise be necessary. If parallel resistance is removed from the circuit, the parallel resistance can be considered to be infinite and equations A.1 and A.2 simplify to the following:

$$i_a(i_b) = i_b \quad (\text{A.4})$$

$$V_a(i_b) = R_s i_b + V_b \quad (\text{A.5})$$

A  $1\Omega$  resistor connected in series when charging the whole battery or a single cell was determined to be adequate. Figure A.17 shows that two sets of 100W  $1\Omega$  power resistors are connected in series with battery. Each set consists of two resistors connected in parallel. Since each of the two sets has an equivalent resistance of  $0.5\Omega$ , total equivalent resistance connected in series with the battery is  $1\Omega$ .

### A.5.3 Amplifier Configuration and Settings

In addition to the external power resistor circuit, the amplifier was configured to minimize internal heat generation and maximize current capacity. The LVC 5050 has three operating modes: stereo (two channel), bridge mono, and parallel mono. The amplifier was set to parallel mode since this operating mode uses both channels to effectively double the current capacity of a single channel. Aside from setting a three point switch on the rear panel of the amplifier to “Parallel”, the

positive terminals of both channels are shorted to engage parallel mode (the negative terminals are always tied together and do not need to be externally shorted as well).

To minimize internal heat generation, the LVC 5050 shifts between high and low impedance modes for high voltage and high current conditions, respectively. The amplifier automatically switches between these different impedance modes by monitoring output current and voltage levels. Alternatively, a particular impedance state (high or low) can be locked. Since the amplifier does not need to supply high voltages for any type of battery testing, the amplifier is locked in a low-impedance state to ensure the internal amplifier impedance is always as small as possible.

## A.6 Voltage, Current, and Pressure Control

The PBTM is capable of controlling amplifier voltage, battery voltage, battery current, or battery pressure. With the exception of the battery pressure controller, each modes use a PI controller with a feedforward signal. Amplifier voltage can be controlled directly whereas controlling battery current or battery voltage require simple plant models.

Controlled battery voltage mode is only used during battery charging. During charging, a  $1\Omega$  resistor is connected in series with the battery. Equation A.6 shows that amplifier voltage, is equal to sum of the battery voltage plus the voltage drop across the  $1\Omega$  resistor.

$$V_a = V_b + V_{1\Omega} \tag{A.6}$$

The voltage drop across the  $1\Omega$  resistor is found by taking the difference between the amplifier and battery voltages. Equation A.6 becomes:

$$V_a = V_b + (V_{a_{measured}} - V_{b_{measured}}) \tag{A.7}$$

It is important to note that  $V_b$  in Equation A.7 represents the output signal from the PI controller

and  $V_a$  is the commanded amplifier voltage.

Controlled battery current mode uses equation A.1 and A.5 during discharging and charging, respectively, as the plant models to convert from a desired current to amplifier voltage.

The PBTM can also control the rate at which gassing pressure increases within a cell. Gassing pressure is controlled through the use of a two-stage controller. In the first stage, a PD controller with integral-like logic tracks a pressure derivate setpoint,  $\dot{P}_{setpoint}$ . The output of the first stage controller is an instantaneous current set point. By continually adjusting the current set point, the first-stage controller is able to track the pressure derivative set point. A reactive PD controller with integral-like logic was chosen because no model of the gassing process was readily available. In the second stage, a PI controller ensures that the actual battery current is tracking the moving current set point that is commanded by the first stage controller.

The first stage controller does not include conventional integral action because the pressure within a given cell cannot be decreased. Relative to the rate at which gassing pressure increases, the recombination and leaking rates are orders of magnitude slower. From a controller design perspective, the pressure within a given cell can only be increased. In other words,  $\dot{P}$  can only be actively controlled in the positive direction.

The first stage PD controller with integral-like control logic behaves much like a conventional PID controller. The set point for  $\dot{P}$  is multiplied by the time signal to find the instantaneous  $P$  set point, which is a ramp signal since the  $\dot{P}$  set point is constant. The continually increasing  $P$  set point is controlled by a conventional PD controller. The control signal is added to the initial current set point to produce the instantaneous current set point. Every five minutes the instantaneous current set point is compared to a 500 second moving average of the current signal. If the current set point differs from the moving average by more than 10%, the set point is either decreased or increased by 10%, depending on whether the difference is positive or negative, respectively. The logic only executes once every 5 minutes because the dynamics of the battery gassing process are sufficiently slow that continual execution of the integral control logic would

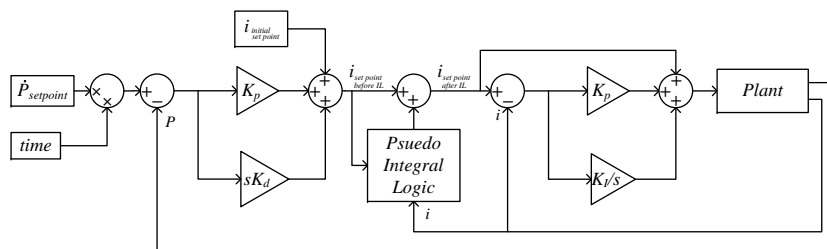


**Figure A.18.** The gassing pressure controller consists of two separate control loops. The first controller tracks a pressure derivative set point by varying the current set point. The second tracks the current set point.

create a widely unstable controller.

The guage pressure signals used to measure gassing pressure within each cell were adjusted in various ways to account for the effects of fluctuations in temperature, atmospheric pressure, and leakage rates. Changes in atmospheric pressure affect guage pressure, but do not influence absolute pressure. Thus, guage pressures and atmospheric pressure signal were combined to find the absolute pressure within each cell. The absolute pressure, rather than the guage pressure, was then used as the pressure feedback signal. Absolute pressure sensors were not initially used to measure cell pressure, even though absolute pressure was ultimately calculated and used as the feedback signal, because each battery chamber has an pressure relief valve that opens when the guage pressure within the cell is approximately 2 psi. If the relief values opens, gas escapes to the atmosphere, making pressure control impossible. Thus, monitoring guage pressure as well as the absolute pressure within each cell is necessary.

The effect of gas leakage on the absolute pressure signal was addressed by predicting gas leakage rates at each guage pressure. The pressure sensors were connected to each cell and pressurized with air to approximately 1 psi. The pressure in each chamber was monitored over the next 24 hours. Leakage rates slowed as guage pressure decreased. An exponential curve was fit to the absolute pressure data. The function was used to add the predicted loss in guage pressure due to leakage to the actual absolute pressure to yield a corrected absolute pressure signal.

The pressure of a gas within a fixed volume also changes with temperature. Since temperature data for each cell was unavailable, the affect of temperature was estimated. Before adding atmospheric pressure to guage pressure to find absolute cell pressure, cell 1 guage pressure was subtracted from cell 3 guage pressure. Cell 1 showed the slowest leakage rates and was therefore, the best approximation for a guage pressure signal with no leakage. Thus, the changes in cell pressure in cell 1 were approximately only due to changes in temperature (changes in atmospheric pressure canceled since these changes affect cell 1 and 3 equally). By subtracting cell 1 guage pressure from that of cell 3, the effects of temperature change on cell 3 guage pressure were nearly eliminated.

## A.7 Impedance Measurement

The most common form of EIS measurement is known as the Frequency Response Analyzer (FRA) method, in which a small AC voltage between 5 to 15mV is induced and the resulting AC current is measured [28]. Precisely and accurately measuring these small voltage fluctuations makes the generation of high fidelity, noise-free EIS plots somewhat challenging. Significantly increasing the amplitude of these small voltage fluctuations is not practical, as this would cause unacceptably large increases in current. A very large current response to a small voltage input can be attributed to the small impedance of batteries.

Despite the availability of EIS machines from several different manufacturers, there currently are no off-the-shelf products capable of characterizing multiple batteries or multiple cells within a single battery simultaneously (to the best of the author's knowledge). As a result, the PBTM was designed to include this capability.

The PBTM is designed for testing 12V lead-acid batteries (Although the machine is capable of testing other types of batteries as well). It has six EIS channels so that it can measure the impedance of each of the six cells within a 12V lead-acid battery.

The machine uses the FRA method to measure EIS. Testing is performed in controlled amplifier voltage mode. The amplifier voltage is set to the battery OCV and then a relay connects the amplifier and battery. Typically a few milliamps of current flow between the battery and amplifier due to a slight voltage imbalance. The amplifier voltage is adjusted slightly until there is no current flow. Next, a sinusoidal voltage is superimposed onto the DC amplifier signal. Sinusoidal fluctuations in battery voltage and current are observed. The amplifier signal amplitude is increased until the amplitude of battery voltage reaches some desired value. The amplifier signal frequency is varied from 0.01Hz to 100Hz.

The AC component of the battery voltage signal is very small and noisy, which results in poor quality EIS plots. To improve signal quality, a circuit was designed to remove the DC offset of each battery voltage signal and amplify the remaining sine wave. This practice is known as level shifting and amplifying. Amplifying a signal will not improve the signal to noise ratio (SNR), but will in fact amplify any noise present along with the signal of interest. Level shifting and amplifying is advantageous because the analog signal uses a larger range of the input channel, which improves voltage resolution. The quantization error is reduced and the Signal-to-quantization-noise ratio (SQNR) can improve dramatically depending on the degree of amplification.

An inverting operational amplifier is used to level shift and amplify battery voltage signals. Figure A.19 shows that the non-inverting (+) input of the op-amp is not grounded (as is typically the case), but connected to a reference voltage. Applying a reference voltage at the non-inverting (+) input shifts the DC offset of the output signal. The value of this reference voltage that eliminates the DC offset can be calculated using the two “golden rules” of op-amps. Deriving an equation for the output voltage (equation A.8) and then solving for the reference voltage (equation A.9) reveals that a 2V DC offset, for example, would be completely eliminated by applying a 1.905V DC signal at the non-inverting input of an op-amp.

$$V_{out} = \frac{V_{ref}(R_f + R_{in}) - V_{in}R_f}{R_{in}} \quad (\text{A.8})$$

$$V_{ref} = \frac{R_{in}V_{out} + R_fV_{in}}{R_{in} + R_f} = \frac{(10k\Omega)(0) + (200k\Omega)(2V)}{10k\Omega + 200k\Omega} = 1.905V \quad (\text{A.9})$$

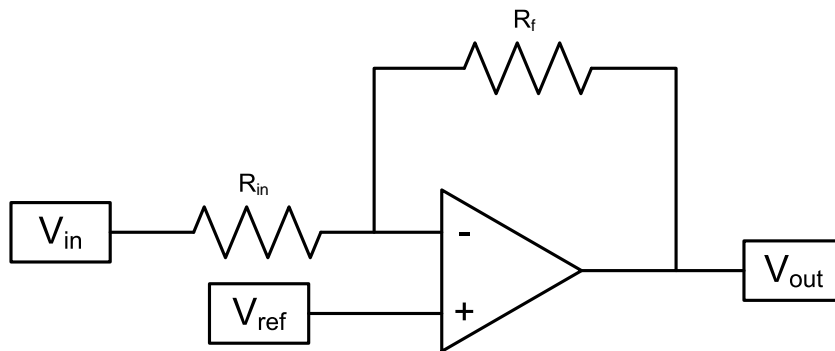


**Figure A.19.** Inverting op-amp with reference signal at non-inverting input

Several PCBs were designed to level shift and amplify the battery voltage signal; however, the first two designs failed. The following sections explain the design errors in the initial iterations and why the final design was successful.

### A.7.1 First Generation EIS Circuit

The first generation PCB failed to produce accurate EIS plots because the actual battery voltage was not measured. Amplifier voltage was divided by battery current to find the total impedance of battery-testing-hardware system. Testing hardware here refers to the wires, current sensors, and relays connected along the current conducting path between the amplifier and battery. Because these components each have some resistance, the impedance that was measured using amplifier voltage represents the sum of battery impedance plus testing hardware resistance. The resistance of the testing hardware was measured by shorting the leads that typically connect to the battery and by connecting the leads that typically connect to the amplifier to a benchtop multimeter.

Equations A.10 shows that battery impedance was obtained by subtracting the resistance of the testing hardware from the total measured impedance of the system.

$$Z_{battery} = Z_{measured} - R_{hardware} \quad \text{where} \quad Z_{measured} = \frac{V_{amplifier}}{i_{battery}} \quad (\text{A.10})$$

This method of measurement was unsuccessful primarily because the resistance of the testing hardware was constantly changing and could not be accurately measured. Slightly moving or touching external wires that connected the battery to the amplifier revealed that wire resistance could change by as much as tens of milli-ohms. Relative to battery impedance, which is usually only a few milli-ohms, this change in wire resistance was very significant. Variation in the resistance of the power relays also contributed to an ever-changing testing hardware resistance. The resistance of the contacts changed each time the relay was actuated. These fluctuations in resistance of the testing hardware made it practically impossible to accurately measure the real impedance (resistance) of the battery, making this design a failure.

### A.7.2 Second Generation EIS Circuit

The second generation PCB avoided the shortcomings of the first generation design by directly measuring battery voltage, but failed to work for other unforeseen reasons. Figure A.20 shows that the two voltages measured at points A and B relative to the DAQ ground are named  $V_+$  and  $V_-$ , respectively. Battery voltage was measured by subtracting  $V_-$  from  $V_+$ . During EIS measurement, when the AC component of  $V_+$  is the signal of interest,  $V_+$  is level shifted and amplified. The amplified, zero-mean signal is read into the ADC input channel. Within Simulink, the amplified voltage is scaled down to its correct value.  $V_-$  is then subtracted from the correctly scaled signal to find the AC battery voltage. Despite the level shifting and amplification, this method produces noisy battery voltage signals.

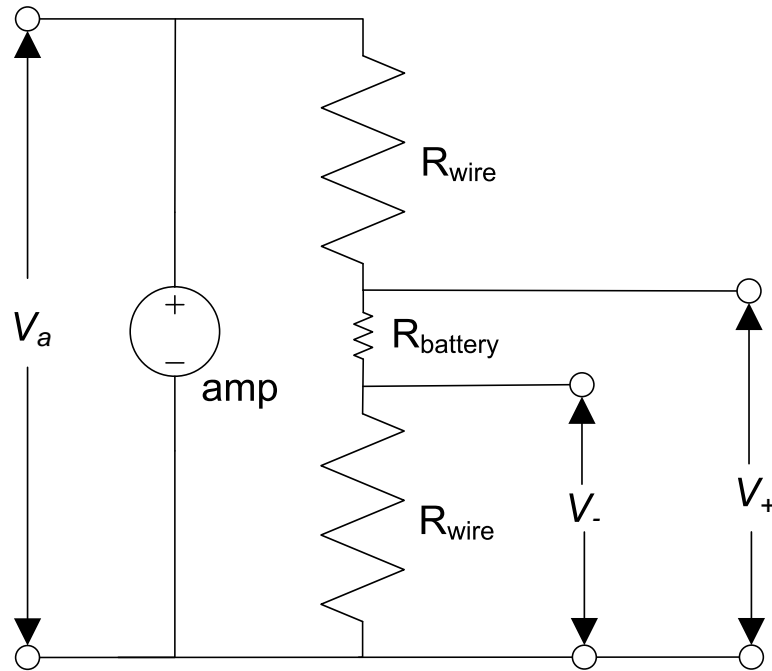


**Figure A.20.** Battery Voltage Measurement.

One of the problem with this approach is that it neglects the resistance of the wires connecting the battery to the amplifier. The resistance of the wires is actually two to three orders of magnitude greater than that of the battery. Therefore, the AC component of  $V_+$  is mostly due to the resistance of the the wire and only slightly due to the resistance of the battery. Figure A.20 shows that the AC signal  $V_-$  is induced solely by the resistance of the wire connecting the negative terminal of the battery to the amplifier ground. Figure A.21 shows that the AC component of  $V_+$  is just the sum of  $V_-$  plus the relatively small voltage oscillations due to the battery. As a result, the amplitude of the AC component of  $V_+$  is only slightly larger than that of  $V_-$ . The difference between these two signals represents the voltage oscillations induced by the battery.

This measurement approach fails because the battery voltage signal is essentially hidden within the  $V_+$  signal, and cannot be amplified by a significant amount. The gain is relatively small ( $G \approx 10$ ) because  $V_+$  is relatively large, and large gains will cause the signal's voltage to

exceed the measuring range of the ADC input channels. Therefore, the battery voltage signal is still very small after  $V_-$  is subtracted from the level-shifted and amplified  $V_+$  signal.

To allow for greater amplification,  $V_-$  was added to  $V_{ref}$ . Typically,  $V_{ref}$  is just a DC signal. In this case, however, the reference signal is the sum of two signals: the DC signal need to remove the input signal DC offset and  $V_-$ . For the purposes of conceptual understanding,  $V_{ref}$  can be loosely thought of as the voltage, relative to which the input signal is being measured. Therefore,  $V_+$  relative to the sum of  $V_-$  plus the DC battery voltage is a zero-mean AC signal that represents battery voltage oscillations. This idea worked perfectly in principle, but poorly in reality. Although the batter voltage oscillations could be amplified by a much larger gain, the signal remained very noisy. The poor signal quality originated from  $V_{ref}$ . The analog  $V_-$  signal need to be converted to a digital signal, added to a DC value in Simulink, and then converted back to an analog signal ( $V_{ref}$ ). Because the signal was converted from the analog to digital and then back from digital to analog, and because these conversions did not occur instantaneously,  $V_{ref}$  suffered from quantization error and time delay. As a result, the battery voltage signal was very noisy.

### A.7.3 Third Generation EIS Circuit

The third generation design solved the problems inherit in earlier designs through the use of instrumentation amplifiers. Instrumentation amplifiers allow the voltage difference between two points to be measured relative to any reference voltage. An instrumentation amplifier was incorporated into the design to subtract the voltage difference between the positive and negative cell electrodes and output a cell voltage signal relative to the DAQ ground. The cell voltage signal is then level shifted and amplified. The importance of isolating the cell voltage signal before level shifting and amplifying cannot be understated. An isolated cell voltage signal can be amplified by a very large gain, since the AC component of the signal is very small. Large amplification leads to a dramatic increase in signal quality. Furthermore, an isolated signal uses a DC reference

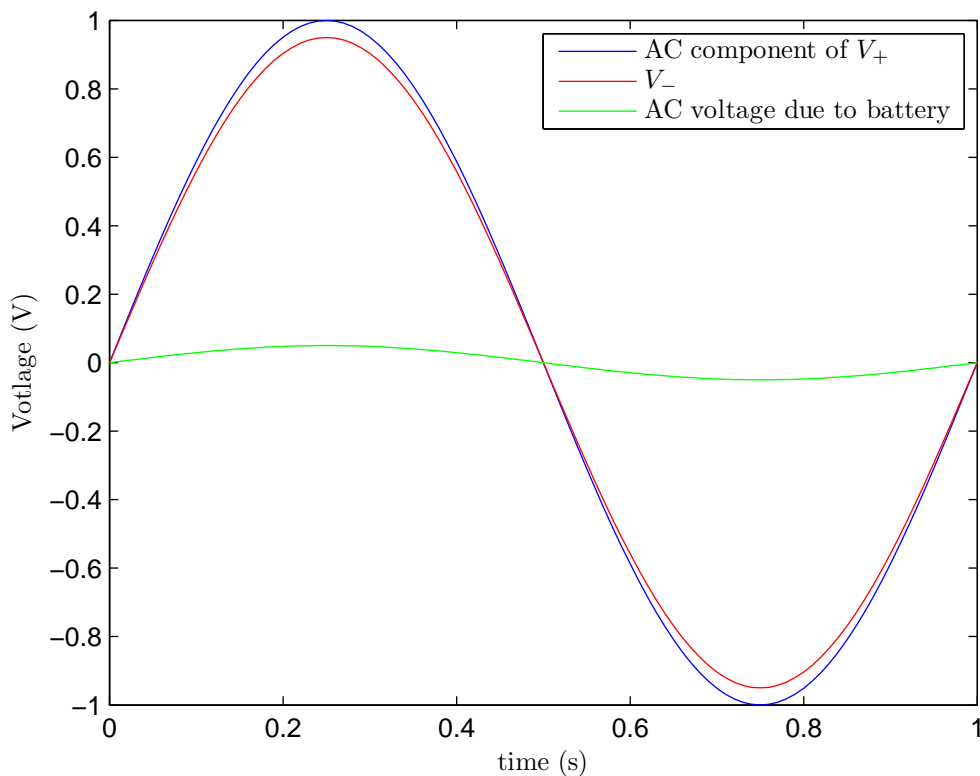


**Figure A.21.** Battery Voltage Amplitude and Raw Signal Amplitudes.

voltage for level shifting. This avoids the complications associated with the combined AC/DC reference voltage signals that plagued the previous design. All of these improvements over the course of three designs ultimately contributed to final circuit's ability to generate noise-free EIS plots.

The success of final design can be attributed in large part to the dramatic amplification of the AC battery voltage. Since the battery voltage amplitude can be as large as 10mV and since the DAQ input can measure signals ranging from -10V to 10V, the battery voltage signal can be amplified by a gain as large as  $G = 1000$ . To avoid any chance of clipping, a gain of  $G = 500$  is chosen. Considering that the input and feedback resistors of a practical op-amp must not be smaller than a few killohmms or larger than a few hundred killohmms [31], the maximum

gain of a single op-amp is approximately  $G = 250$ , if  $R_i = 2k\Omega$   $R_f = 500k\Omega$  are assumed to represent the limits of the practical op-amp range. Therefore, to avoid exceeding the resistance recommendations, amplification is divided into two stages. In the first stage, an inverting op-amp with a reference signal at its non-inverting input removes the DC offset and amplifies the signal by a gain of  $G = 20$ . A second inverting op-amp amplifies the output of the first stage by an additional gain of  $G = 25$ . Thus the total amplification of both stages is  $G = 500$ . It is important to note the second stage op-amp is a conventional inverting op-amp and does not level-shift the signal since this is already done in the first stage.

## A.8 Safety Features

Several features are incorporated into the design of the hardware to ensure safe operation. A 20A removable fuse and pull-button emergency stop are connected between the battery and amplifier. A 3A removable fuse is connected along the 120AC mains line. All power relays are the non-latching and normally-open type. In the event of a power failure, all relays will switch open and disconnect the battery from the amplifier and any resistors.

Safeguards are built into the software as well. Currents exceeding a predefined value in ControlDesk will automatically open the main connection relay and disconnect the battery from the circuit. The same relay can be programmed to open if cell pressure exceeds a certain value, if current falls below a predefined lower bound, or if cell (or battery) voltage exceeds a certain limit.

# Appendix B

## Circuit Diagrams

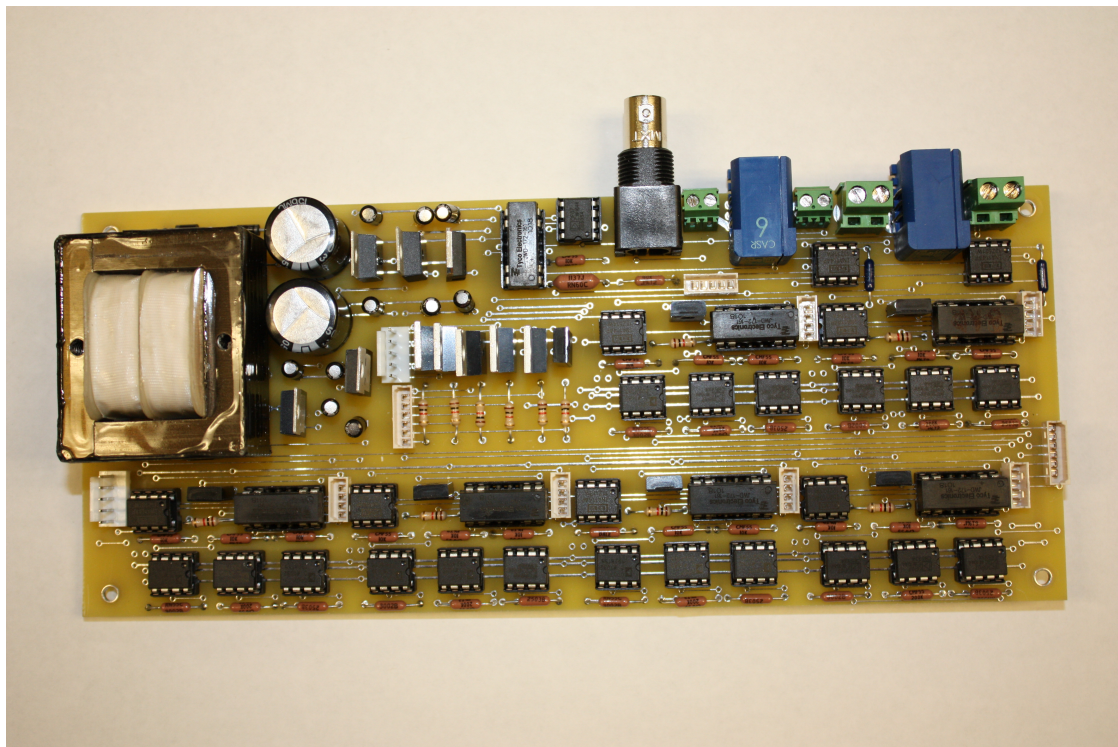


Figure B.1. Picture of PCB



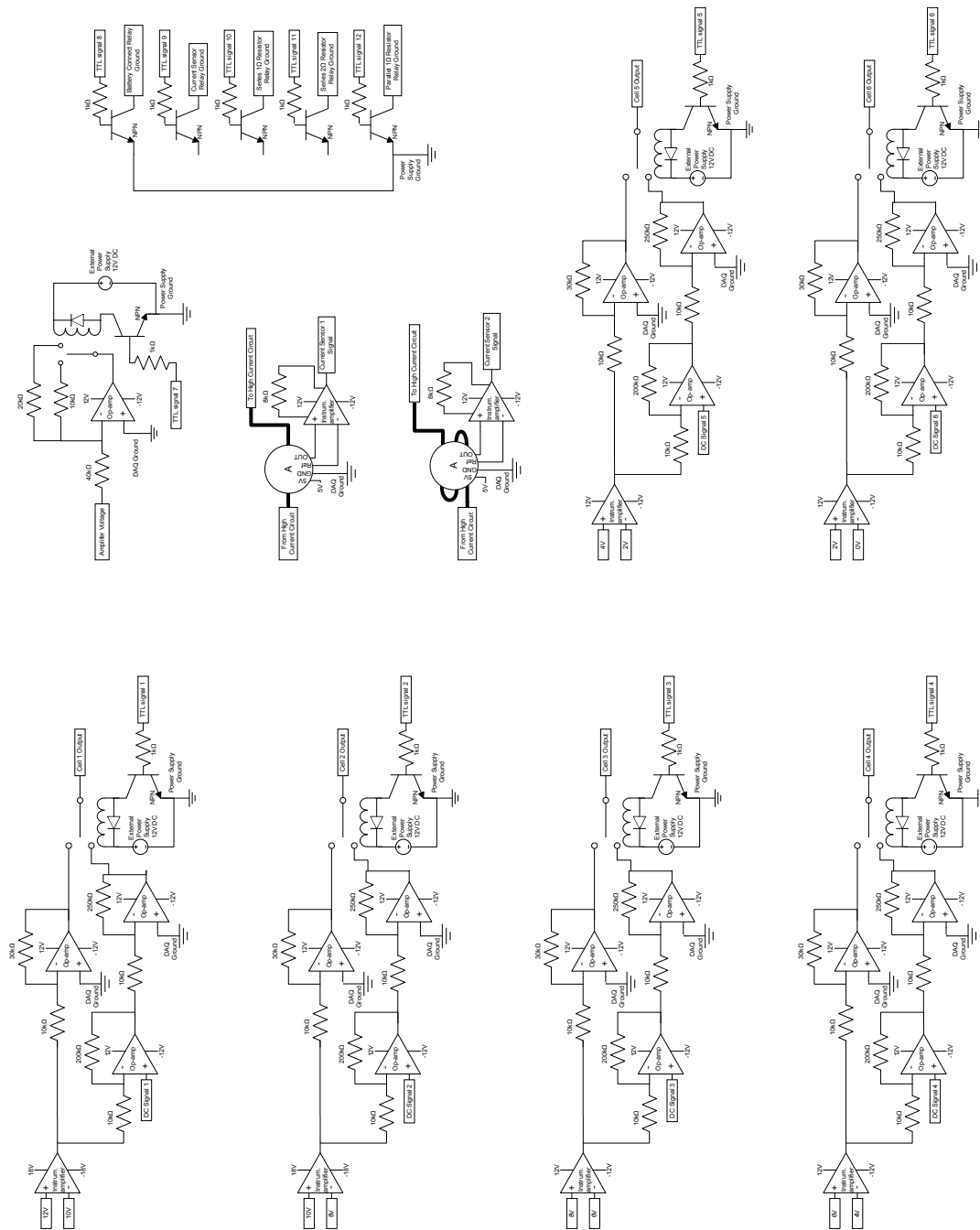


Figure B.3. Diagram of Circuits on PCB

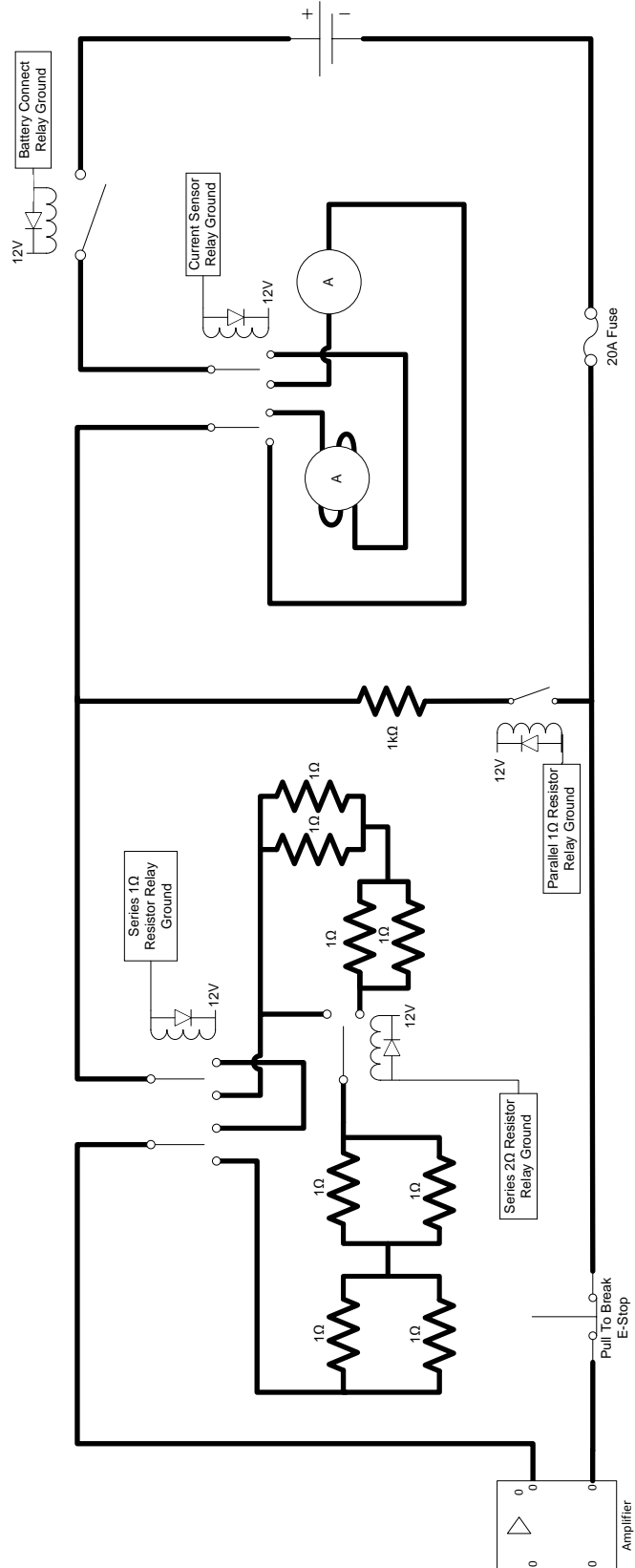


Figure B.4. High level view of PBTM.

# Bibliography

- [1] SCHIFFER, J., D. U. SAUER, H. BINDNER, T. CRONIN, P. LUNDSAGER, and R. KAISER (2007) “Model prediction for ranking lead-acid batteries according to expected lifetime in renewable energy systems and autonomous power-supply systems,” *Journal of Power Sources*, **168**(1), pp. 66 – 78.
- [2] BINDNER, H., T. CRONIN, P. LUNDSAGER, J. MANWELL, U. ABDULWAHID, and I. BARING-GOULD (2005) *Lifetime Modelling of Lead Acid Batteries*, Tech. Rep. Risø-R-1515(EN), RisøNational Laboratory, Denmark.
- [3] CULPIN, B. and D. RAND (1991) “Failure modes of lead/acid batteries,” *Journal of Power Sources*, **36**(4), pp. 415 – 438.
- [4] GIBSON, I. and K. PETERS (1982) “Sulphation in discharged lead-acid batteries,” *Journal of Power Sources*, **8**(2), pp. 143 – 157.
- [5] YAMAGUCHI, Y., M. SHIOTA, Y. NAKAYAMA, N. HIRAI, and S. HARA (2000) “In situ analysis of electrochemical reactions at a lead surface in sulfuric acid solution,” *Journal of Power Sources*, **85**(1), pp. 22 – 28.
- [6] TAKEHARA, Z. (2000) “Dissolution and precipitation reactions of lead sulfate in positive and negative electrodes in lead acid battery,” *Journal of Power Sources*, **85**(1), pp. 29 – 37.
- [7] KIM, U. S., C. B. SHIN, S. M. CHUNG, S. T. KIM, and B. W. CHO (2009) “Modeling of the capacity loss of a 12V automotive lead-acid battery due to ageing and comparison with measurement data,” *Journal of Power Sources*, **190**(1), pp. 184 – 188, selected Papers presented at the 11th ULM ElectroChemical Days.
- [8] CHERIF, A., M. JRAIDI, and A. DHOUB (2002) “A battery ageing model used in stand alone PV systems,” *Journal of Power Sources*, **112**(1), pp. 49 – 53.
- [9] LAM, L., N. HAIGH, C. PHYLAND, and A. URBAN (2004) “Failure mode of valve-regulated lead-acid batteries under high-rate partial-state-of-charge operation,” *Journal of Power Sources*, **133**(1), pp. 126 – 134, proceedings of the Tenth Asian Battery Conference.
- [10] SCHAECK, S., T. KARSPECK, C. OTT, M. WECKLER, and A. STOERMER (2011) “A field operational test on valve-regulated lead-acid absorbent-glass-mat batteries in micro-hybrid electric vehicles. Part I. Results based on kernel density estimation,” *Journal of Power Sources*, **196**(5), pp. 2924 – 2932.

- [11] SCHAECK, S., T. KARSPECK, C. OTT, D. WEIRATHER-KOESTNER, and A. STOERMER (2011) “A field operational test on valve-regulated lead-acid absorbent-glass-mat batteries in micro-hybrid electric vehicles. Part II. Results based on multiple regression analysis and tear-down analysis,” *Journal of Power Sources*, **196**(5), pp. 2933 – 2938.
- [12] PILLER, S., M. PERRIN, and A. JOSSEN (2001) “Methods for state-of-charge determination and their applications,” *Journal of Power Sources*, **96**(1), pp. 113 – 120, [; Proceedings of the 22nd International Power Sources Symposium](http://www.sciencedirect.com/science/article/pii/S0378775301005602).
- URL <http://www.sciencedirect.com/science/article/pii/S0378775301005602>
- [13] BHANGU, B., P. BENTLEY, D. STONE, and C. BINGHAM (2005) “Nonlinear observers for predicting state-of-charge and state-of-health of lead-acid batteries for hybrid-electric vehicles,” *Vehicular Technology, IEEE Transactions on*, **54**(3), pp. 783 – 794.
- [14] GOULD, C., C. BINGHAM, D. STONE, and P. BENTLEY (2009) “New Battery Model and State-of-Health Determination Through Subspace Parameter Estimation and State-Observer Techniques,” *Vehicular Technology, IEEE Transactions on*, **58**(8), pp. 3905 – 3916.
- [15] FAIRWEATHER, A., M. FOSTER, and D. STONE (2011) “Battery parameter identification with Pseudo Random Binary Sequence excitation (PRBS),” *Journal of Power Sources*, **196**(22), pp. 9398 – 9406.
- URL <http://www.sciencedirect.com/science/article/pii/S0378775311013097>
- [16] HUET, F. (1998) “A review of impedance measurements for determination of the state-of-charge or state-of-health of secondary batteries,” *Journal of Power Sources*, **70**(1), pp. 59 – 69.
- URL <http://www.sciencedirect.com/science/article/pii/S0378775397026657>
- [17] VISWANATHAN, V. V., A. J. SALKIND, J. J. KELLEY, and J. B. OCKERMAN (1995) “Effect of state of charge on impedance spectrum of sealed cells Part II: Lead acid batteries,” *Journal of Applied Electrochemistry*, **25**, pp. 729–739, [10.1007/BF00648628](https://doi.org/10.1007/BF00648628).
- URL <http://dx.doi.org/10.1007/BF00648628>
- [18] MAURACHER, P. and E. KARDEN (1997) “Dynamic modelling of lead/acid batteries using impedance spectroscopy for parameter identification,” *Journal of Power Sources*, **67**(1-2), pp. 69 – 84, proceedings of the Fifth European Lead Battery Conference.
- [19] BULLER, S., M. THELE, E. KARDEN, and R. W. D. DONCKER (2003) “Impedance-based non-linear dynamic battery modeling for automotive applications,” *Journal of Power Sources*, **113**(2), pp. 422 – 430, proceedings of the International Conference on Lead-Acid Batteries, LABAT '02.
- [20] THELE, M., E. KARDEN, E. SUREWAARD, and D. SAUER (2006) “Impedance-based overcharging and gassing model for VRLA/AGM batteries,” *Journal of Power Sources*, **158**(2), pp. 953 – 963, special issue including selected papers from the 6th International Conference on Lead-Acid Batteries (LABAT 2005, Varna, Bulgaria) and the 11th Asian Battery Conference (11 ABC, Ho Chi Minh City, Vietnam) together with regular papers.
- [21] BLANKE, H., O. BOHLEN, S. BULLER, R. W. D. DONCKER, B. FRICKE, A. HAMMOUCHE, D. LINZEN, M. THELE, and D. U. SAUER (2005) “Impedance measurements on lead-acid batteries for state-of-charge, state-of-health and cranking capability prognosis in electric and hybrid electric vehicles,” *Journal of Power Sources*, **144**(2), pp. 418 – 425, [; Selected papers from the Ninth European Lead Battery Conference](http://www.sciencedirect.com/science/article/pii/S0378775304011140).
- URL <http://www.sciencedirect.com/science/article/pii/S0378775304011140>

- [22] HAMMOUCHE, A., E. KARDEN, and R. W. D. DONCKER (2004) "Monitoring state-of-charge of Ni-MH and Ni-Cd batteries using impedance spectroscopy," *Journal of Power Sources*, **127**(1-2), pp. 105 – 111, <http://www.sciencedirect.com/science/article/pii/S0378775303009443>
- [23] BUNDY, K., M. KARLSSON, G. LINDBERGH, and A. LUNDQVIST (1998) "An electrochemical impedance spectroscopy method for prediction of the state of charge of a nickel-metal hydride battery at open circuit and during discharge," *Journal of Power Sources*, **72**(2), pp. 118 – 125.  
URL <http://www.sciencedirect.com/science/article/pii/S0378775397026955>
- [24] TROLTZSCH, U., O. KANOUN, and H.-R. TRANKLER (2006) "Characterizing aging effects of lithium ion batteries by impedance spectroscopy," *Electrochimica Acta*, **51**(8-9), pp. 1664 – 1672, <http://www.sciencedirect.com/science/article/pii/S0013468605007899>
- [25] YAZAMI, R. and Y. F. REYNIER (2002) "Mechanism of self-discharge in graphite/lithium anode," *Electrochimica Acta*, **47**(8), pp. 1217 – 1223.  
URL <http://www.sciencedirect.com/science/article/pii/S0013468601008271>
- [26] BOUCHET, R., S. LASCAUD, and M. ROSSO (2003) "An EIS Study of the Anode Li/PEO-LiTFSI of a Li Polymer Battery," *Journal of The Electrochemical Society*, **150**(10), pp. A1385–A1389.  
URL <http://link.aip.org/link/?JES/150/A1385/1>
- [27] ABRAHAM, D. P., S. D. POPPEN, A. N. JANSEN, J. LIU, and D. W. DEES (2004) "Application of a lithium reference electrode to determine electrode contributions to impedance rise in high-power lithium-ion cells," *Electrochimica Acta*, **49**(26), pp. 4763 – 4775.  
URL <http://www.sciencedirect.com/science/article/pii/S0013468604005596>
- [28] BYOUNG-YONG CHANG, S.-M. P. (2010) "Electrochemical Impedance Spectroscopy," *Annual Review of Analytical Chemistry*, **3**, pp. 207–229.
- [29] BERNDT, D. (1997) *Maintenance-free Batteries: Lead-Acid, Nickel/Cadmium, Nickel/Metal Hydride*, Research Studies Press.
- [30] AE TECHRON, 2507 Warren St. Elkhart IN 46516 U.S.A. (2002) *LVC5050 Power Supply Amplifier Technical Manual*.
- [31] J. EDWARD CARRYER, T. K., MATTHEW OHLINE (2010) *Introduction to Mechatronic Design*, Prentice Hall.

## Vita

**Christopher A. Ferone**

### EDUCATION

**M.S. in Mechanical Engineering**, May 2012

The Pennsylvania State University, University Park, PA, 3.79 G.P.A.

*Relevant Graduate Courses:* Advanced Mechatronics, Automatic Control Systems, DSP, Optimal Control of Energy Systems

**B.S. in Mechanical Engineering** with Honors and Distinction, May 2009

The Pennsylvania State University, University Park, PA, 3.76 G.P.A.

Schreyer Honors College

### SKILLS

- MATLAB, Simulink, sensors, microcontrollers, dSPACE/ControlDesk, LabVIEW, machining, PCB design, analog circuit design, SolidWorks, Pro/ENGINEER, AutoCAD, Spanish

### RESEARCH EXPERIENCE

**Master's Thesis Research**, May 2011 - Present

Mechatronics Research Lab, University Park, PA

- Designed and built a machine capable of cycling batteries, measuring battery impedance at various frequencies, and conducting battery desulfation
- Created said machine by designing an embedded circuit and integrating it with current sensors, pressure sensors, relays, power resistors, and power supplies
- Created PI controllers in Simulink capable of controlling battery voltage or current and interfaced Simulink models with dSPACE software and hardware
- Developed a controller that increased the capacity of a degraded battery by 20
- Coauthored *Nondestructive Forensic Pathology of Lead-Acid Batteries*-a paper accepted by the 2012 American Control Conference (ACC) that heavily relied on data provided by the machine I designed and built

### WORK EXPERIENCE

**Wind Turbine Engineer**, May 2009 - August 2009

Princeton Satellite Systems, Plainsboro, NJ

- Designed a 5 kW variable-blade-pitch Vertical Axis Wind Turbine (VAWT)
- Determined how to package a generator, shaft bearings, slip ring, and exterior bearing isolator seal within a compact housing unit using SolidWorks
- Created a model in MATLAB to predict power output and aerodynamic forces on structural members

**Innovation Department Intern**, May 2008 - July 2008  
Johnson Electric APG Europe, Murten, Switzerland

- Investigated the best way to detect, without contact, the functionality of stepper motors mounted on vehicle HVAC units
- Designed a device with motion-sensing lasers to detect motor operation
- Developed a LabVIEW program to map electronic motor addresses to physical locations on HVAC units by individually actuating motors and sensing movement

## VOLUNTEER EXPERIENCE

**Long-term Volunteer**, September 2009 - July 2010  
Amigos de Jess Service Community, Macuelizo, Honduras

- Taught English and computer classes at an orphanage and managed an outreach program that aided poor community members with the cost of medicine and food